Supplementary Information

Complexes $(TBA^{+})\{(TMI\text{-}NPS)_2 \cdot La^{III}I_4)^{-}$ (La = Dy, Tb) with two axial photochromic spiropyran ligands: photoswitching and zero-field SIM behaviour with a high magnetization blocking barrier for the Dy complex

Nikita G. Osipov,[a] Maxim A. Faraonov,[a] Aleksey V. Kuzmin,[b] Salavat S. Khasanov,[b]

Alexey A. Dmitriev,[c] Nina P. Gritsan,[c] Akihiro Otsuka,[d] Hideki Yamochi, [d]

Hiroshi Kitagawa,[d] Dmitri V. Konarev*[a]

Table S1. IR spectra of parent compounds and complexes **1-3**.

Components	TBAI	TMI-NPS	$(TBA^{+})\{(TMI\text{-}NPS)_2{\cdot}Dy^{III}I_4)^{-}\cdot 0.5C_6H_4Cl_2$ (**1**)	$(TBA^{+})\{(TMI\text{-}NPS)_2{\cdot}Tb^{III}I_4)^{-}\cdot 0.5C_6H_4Cl_2$ (**2**)
TMI-NPS		415s	418s	413m
		448s	-	437w
		469m	470s	468s
		496s	-	488m
		521s	515m	520m
		552s	-	551w
		569w	567m	567m
		575m	-	580w
		590s	-	600w
		625m	637m	620w
		648s	-	639m
		671w	668m*	676w
		687s	694w	692m
		733s	736w	734m
		745s	749s*	748s*
		806s	804s	802s
		818s	-	831s
		862s	863m	858m
		935s	930m	-
		949w	949m	947m
		961w	-	968m
		988s	-	997m
		1015s	1019s	1020s
		1024s	1036m*	1037s*
		1082s	1088s	1089s
		1107s	1116s	1115s*
		1142s	1145m	1145m
		1155s	1158s	1157s
		1186s	1194s	1193s
		1209m	1207s	1207s
		1236s	1236s	1235s
		1250s	1251s	1250s
		1279s	1286s	1286s
		1306s	-	-
		1338s	1338s	1338s
		1360s	1362s	1362s
		1379s	1390s	1390s
		1439m	1428m	1429m
		1458s	1450s	1451s
		1489s	1479s	1480s
		1508w	1498m	1498s
		1518m	1524s	1524s
		1560w	1559m	1562s
		1574w	1569m	-
		1587m	1581m	1581s
		1611s	1611w	1612m
		1641s	-	--
		2872w	2872s	2869m
		2930w	2929w	2930w
		2967m	2958s	2959m
		3044m	3046m	3045m
	426w			
	528m		-	422m
	669w		-	-
	735s		668m*	676w*
	797m		736w*	734m*
	881s		804s*	802s*
	924s		875w	-
	991s		930m*	-
	1030s		997m	997m*
	1067s		1036m*	1037s*
	1109s		1116s*	1115s*
	1377s		-	-
	1466s		-	-
	2872s		2872s*	2869m*
	2955s		2958s*	2959m*
		$C_6H_4Cl_2$	$C_6H_4Cl_2$	$C_6H_4Cl_2$
		663w	668m*	660w
		751s	749s*	748s*
Solvent		1035m	1036m*	1037s*
		1120s	1116s*	1115s*
		1462m	1450s*	1451s*

*bands are coincided, sp. – split band, w- weak, m- middle, s- strong intensity.

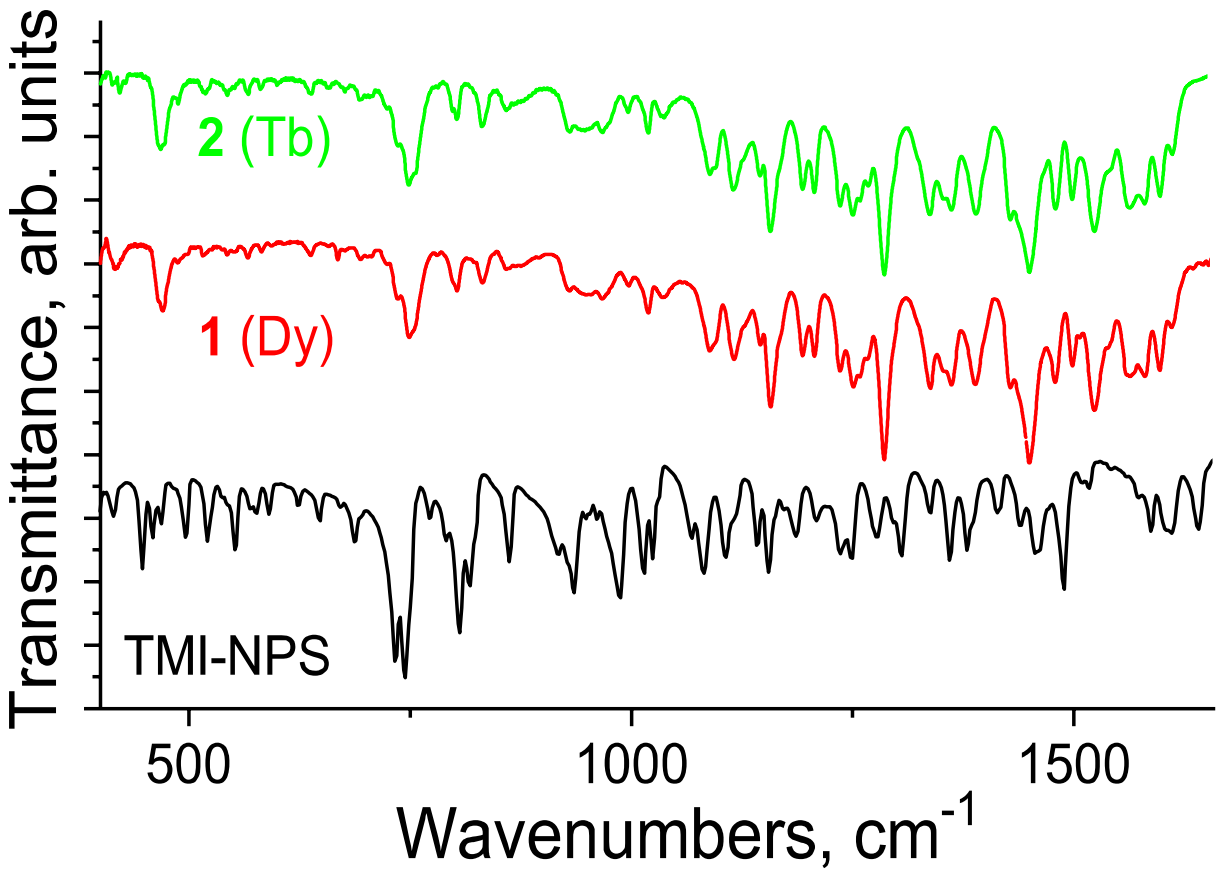

Fig. S1. IR spectra of starting TMI-NPS and $(TBA^{+})\{(TMI\text{-}NPS)_2 \cdot Ln^{III}I_4)^{-} \cdot 0.5C_6H_4Cl_2$ (Ln = Dy (**1**), Tb (**2**)) complexes measured in KBr pellets prepared in anaerobic conditions.

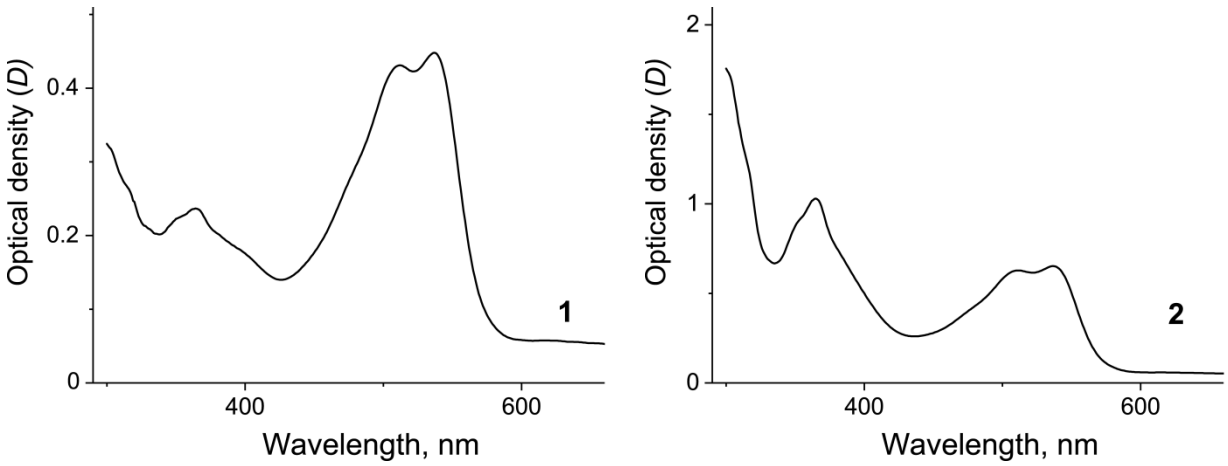

Fig. S2. Electronic absorption spectra measured in *o*-dichlorobenzene under anaerobic conditions when crystals of **1** (left, $C = 3.19\times10^{-5}$ M, $\varepsilon = 1.41\times10^{4}$ L/mol×cm at $\lambda = 538$ nm) and **2** (right, $C = 3.13\times10^{-5}$ M, $\varepsilon = 2.08\times10^{4}$ L/mol×cm at $\lambda = 538$ nm) were dissolved.

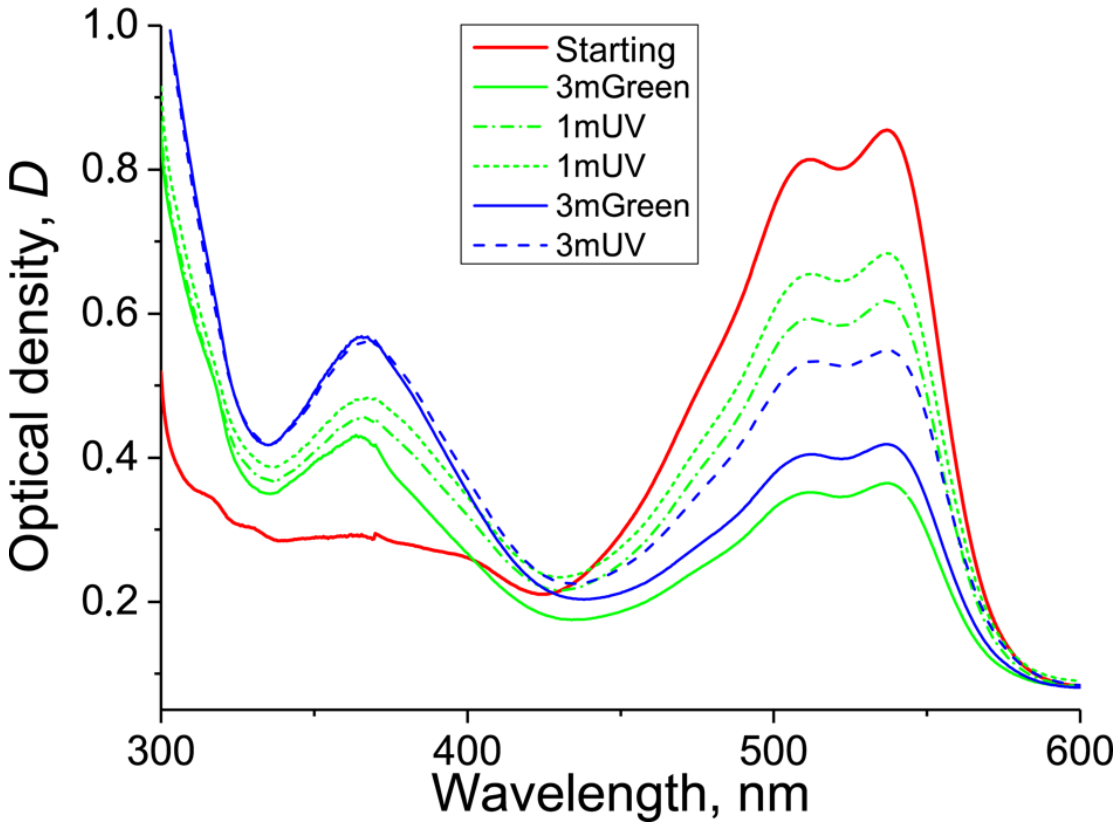

Fig. S3. Two cycles for the photoinduced dissociation and formation of the complex **1** in o-dichlorobenzene solution under green and UV light irradiation. Spectrum of starting solution (red curve), photodissociation of the complex (first cycle – green and second cycle – blue curves) and photoinduced formation of the complex under the UV light excitation (green and blue dashed lines, respectively) in anaerobic conditions in *o*-dichlorobenzene solution.

Crystal structures.

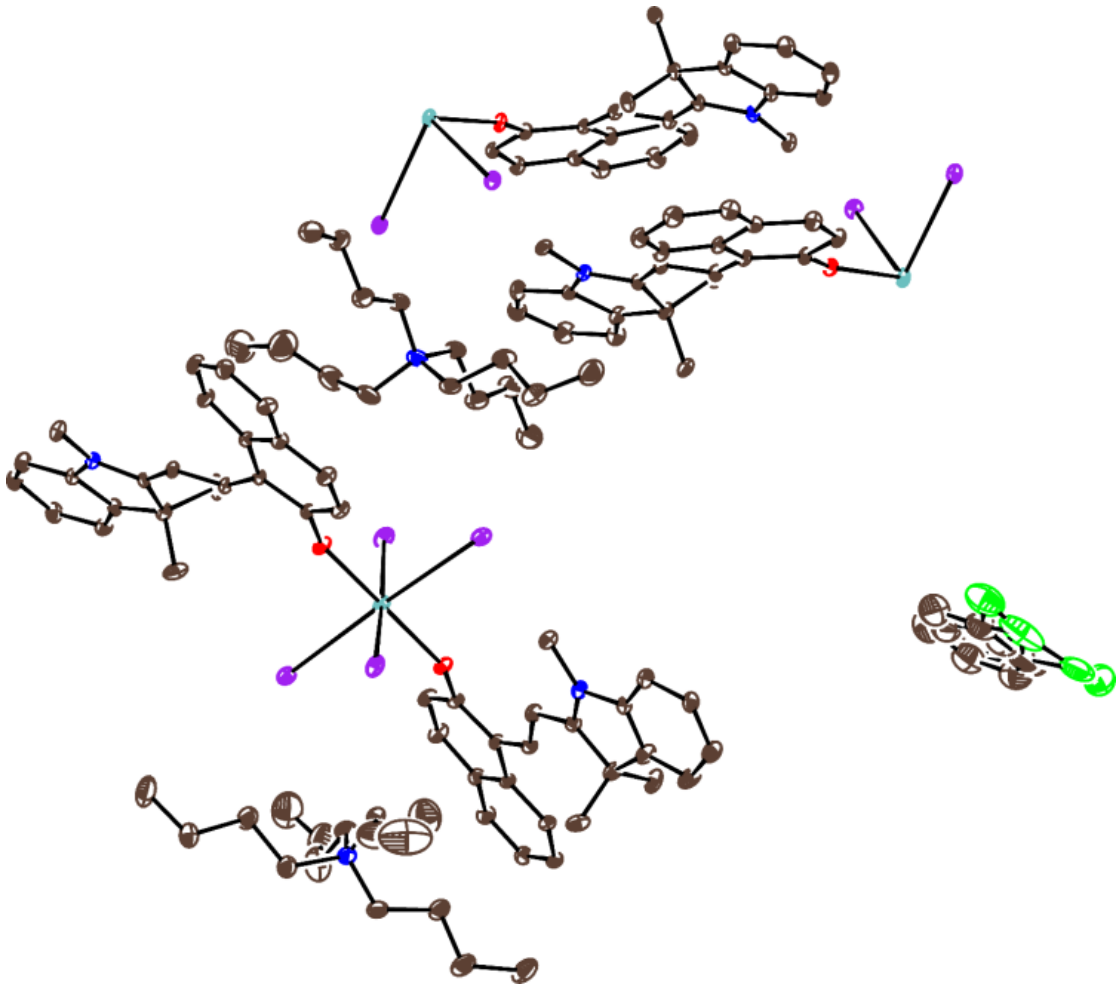

Fig. S4. Crystallographically independent units in the structures of $(TBA^{+})\{(TMI\text{-}NPS)_2{\cdot}Dy^{III}I_4)^{-}{\cdot}0.5C_6H_4Cl_2$ (**1**). One whole and two halves of $\{(TMI\text{-}NPS)_2{\cdot}La^{III}I_4)^{-}$ units are independent. Color code: carbon, brown; oxygen, red; nitrogen, blue; chlorine, green; iodine, violet; dysprosium, greenish-blue, terbium, grey. Ellipsoid probability is 25%. $C_6H_4Cl_2$ molecule is disordered between two positions.

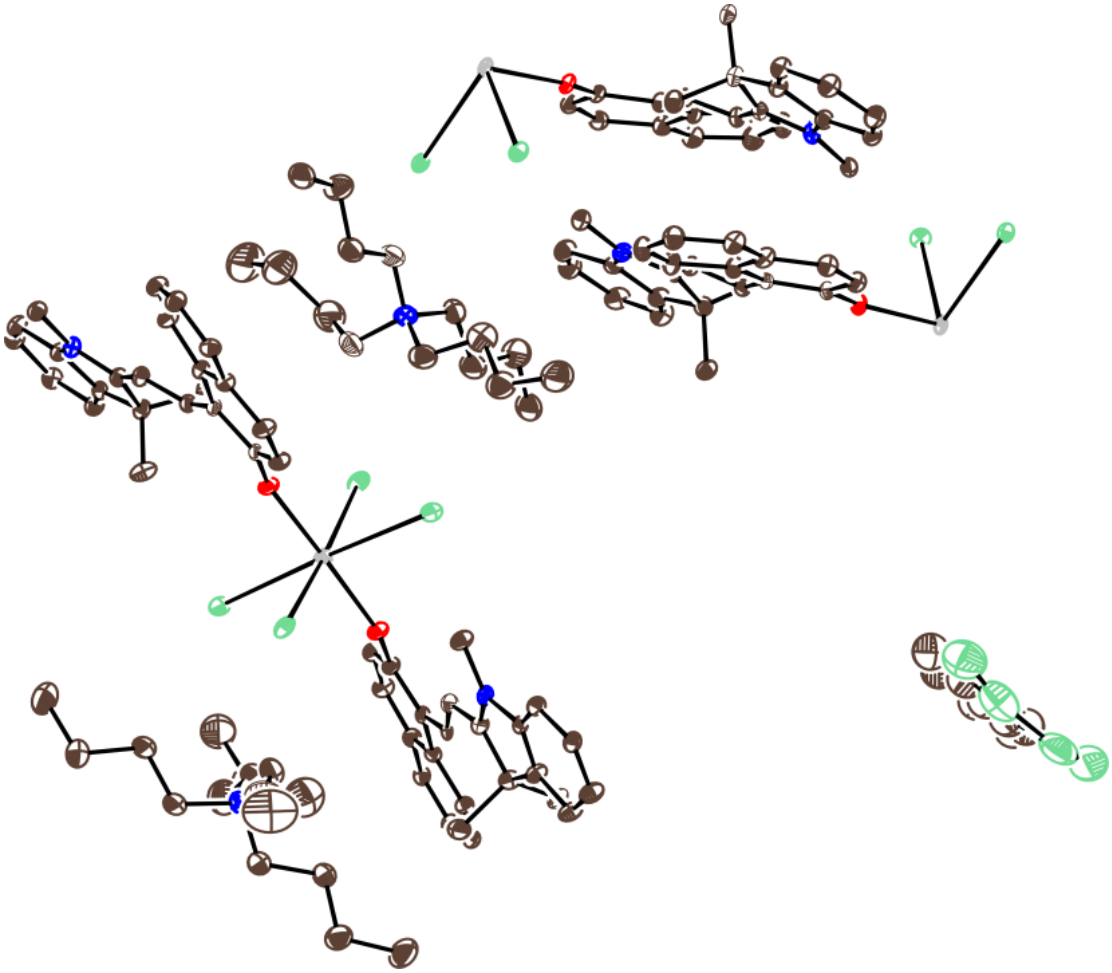

Fig. S5. Crystallographically independent units in the structure of $(TBA^{+})\{(TMI\text{-}NPS)_2{\cdot}Tb^{III}I_4)^{-}{\cdot}0.5C_6H_4Cl_2$ (**2**). One whole and two halves of $\{(TMI\text{-}NPS)_2{\cdot}La^{III}I_4)^{-}$ units are independent. Color code: carbon, brown; oxygen, red; nitrogen, blue; chlorine, green; iodine, violet; dysprosium, greenish-blue, terbium, grey. Ellipsoid probability is 25%. $C_6H_4Cl_2$ molecule is disordered between two positions.

Magnetic properties.

Compound 1: static experimental properties

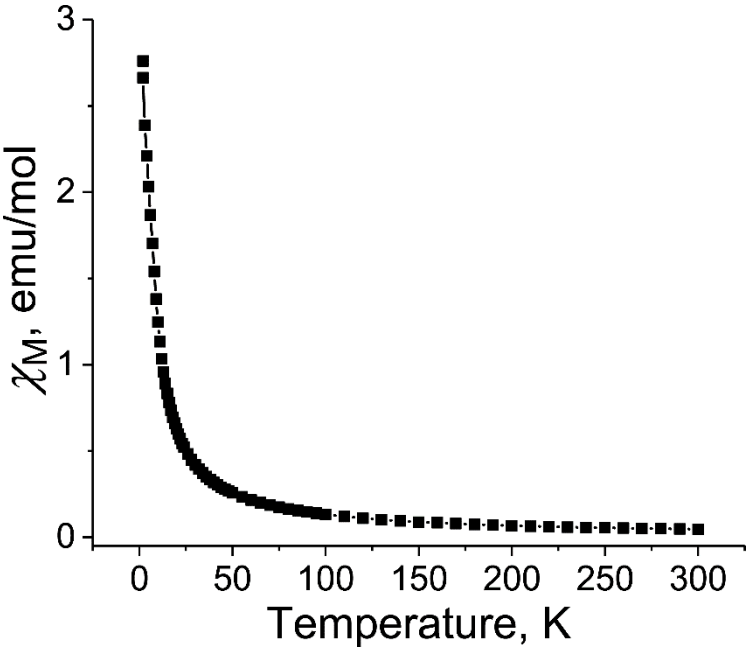

Fig. S6. Data of SQUID measurements for polycrystalline **1**. The temperature dependence of molar magnetic susceptibility is shown in the 1.9-300 K range after the subtraction of a temperature independent contribution.

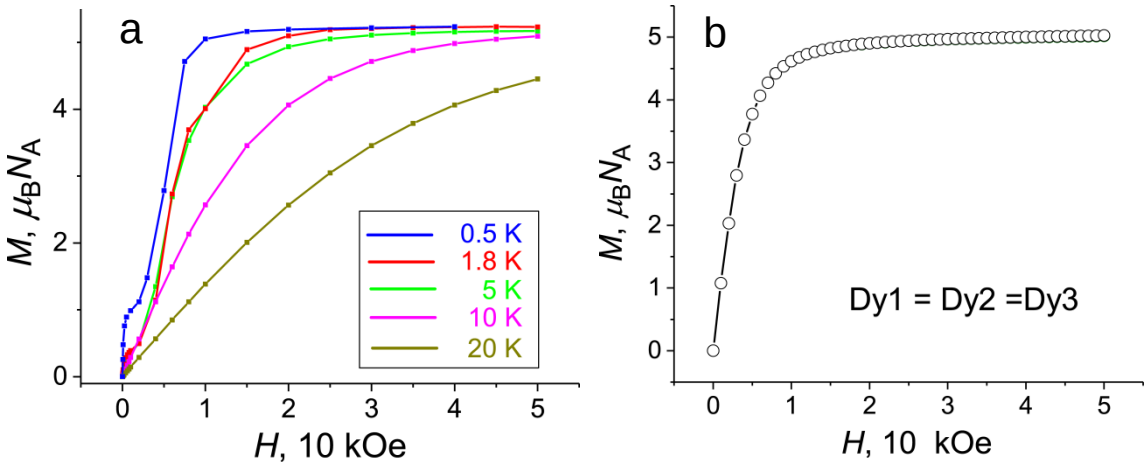

Fig. S7. (a) Field-dependent magnetization for polycrystalline **1** at 0.5, 1.8, 5, 10 and 20 K; (b) High-field powder magnetization at 2K calculated for three structurally different Dy complexes (Dy1-Dy3) using SINGLE-ANISO procedure and results of SA-CASSCF(8,7)/NEVPT2/SOC-QDPT calculations.

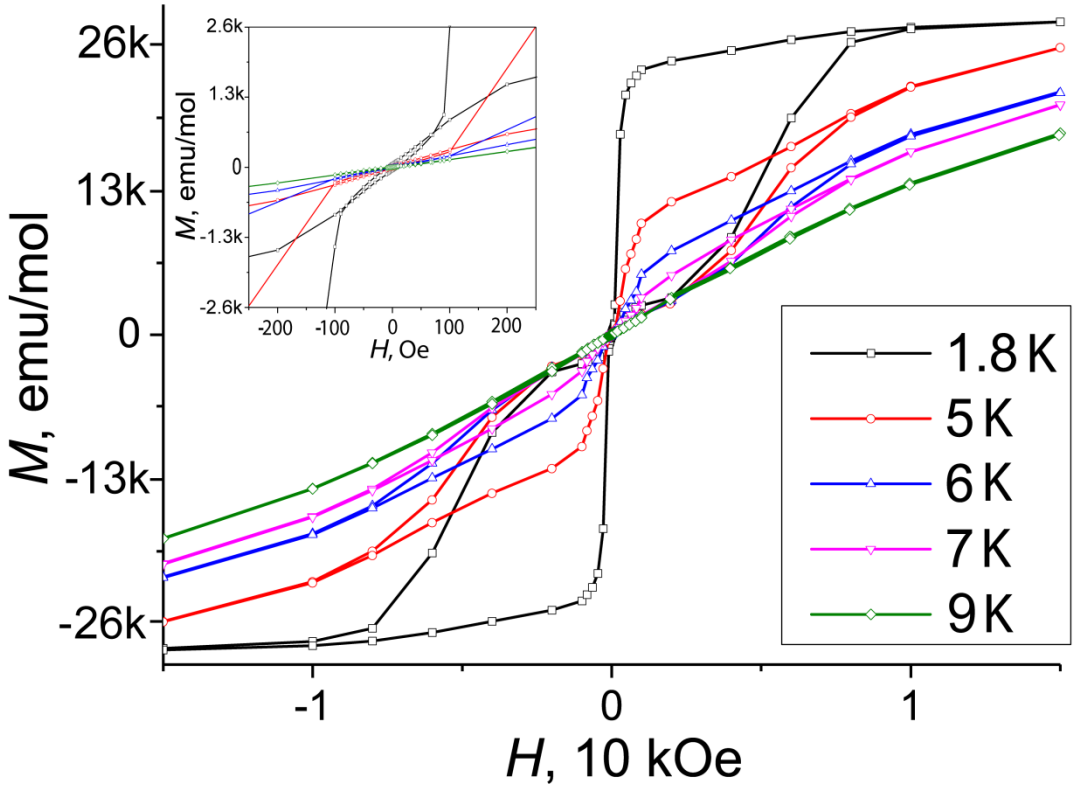

Fig. S8. Hysteresis loops for polycrystalline **1** at 1.8, 5, 6, 7 and 9 K, expanded view of the variable-field magnetization near the zero field (±250 Oe) at the same temperatures. Hysteresis loop is collapsed at 9 K.

Compound 1: dynamic magnetic properties

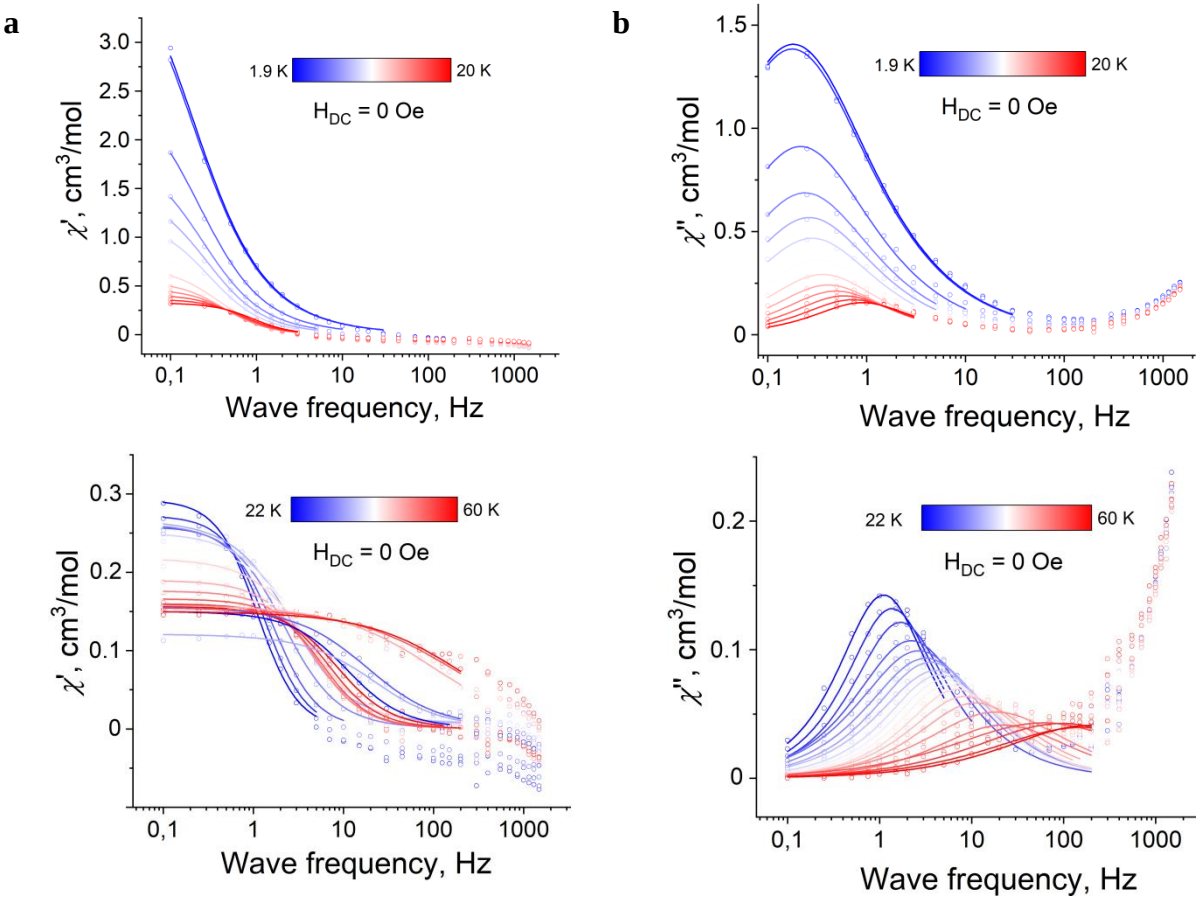

Fig. S9. Frequency dependences of in-phase (χ') (a) and out-of-phase (χ'') (b) AC magnetic susceptibilities for **1** in 0 Oe static magnetic field and temperatures of 1.9 - 60 K. Solid lines represent the fitting of the data by the generalized Debye model.

Theoretical calculations of electronic structure and magnetic properties of complex 1

Computational methodology

For *ab initio* electronic structure calculations discussed in this paper, two similar approaches were used: the first, realized in the OpenMolcas suit of programs (version 21.05) [1], and the second, applied in the ORCA software suit (release 5.0.3) [2]. For complexes containing Dy^{III} cations, the electronic energies and wave functions of spin multiplets (21 sextets, 128 quartets, and 130 doublets) were calculated at the state-averaged [3] (SA) CASSCF(9,7) level [4] (active space: nine electrons distributed over the seven f-orbitals of Dy). For Tb^{III} complexes, calculations of the energies and wavefunctions of seven septet and five quint states were performed with active space consisting of eight electrons distributed over the seven f-orbitals. It has been shown previously that very resource-consuming calculations taking into account 7 septets, 140 quintets, 588 triplets and 490 singlets (namely, all multiplets arising from the f^8 electron configuration) give practically the same results as significantly less resource-consuming calculations taking into account only 7 septets and 5 quintets. For Ce complex, calculations of the energies and wavefunctions of seven doublet states were performed with active space consisting of one electron distributed over the seven f-orbitals.

In the first approach, the relativistic ANO-RCC-VTZP basis set was used for Dy, Tb, I and O atoms, and ANO-RCC-VDZ basis set for all other atoms [5]. In the second approach, SARC2-DKH-QZVP basis set was used for Dy, Tb and Ce, SARC2-DKH-TZVP – for I atom and DKH-def2-tzvp(-f) for all other atoms [6]. The XRD geometries of the complexes were used in all calculations.

In both approaches, scalar relativistic effects were taken into account using the DKH2 Hamiltonian [7]. In the first approach, the spin–orbit coupling (SOC) was treated non-perturbatively within the mean-field theory in the restricted active space state interaction (SO-

RASSI) method [8], in which the CASSCF wave functions are used as the basis states. In the second approach, SOC was taken into account through the use of quasi-degenerate perturbation theory (QDPT) [9]. In both cases, diagonalization of the spin–orbit matrix leads to spin-orbit multiplets: Kramers doublets for Dy^{III} and Ce^{III} complexes and non-Kramers doublets for Tb^{III} complexes. Moreover, the energies of spin multiplets were also clarified by NEVPT2 [10] calculations using ORCA software.

To calculate parameters of the effective spin (pseudospin) Hamiltonians (g-tensors, their principal values, angular momenta along the principal magnetic exes, matrix elements of the transverse magnetic moment, etc.) and the static magnetic properties of complexes with one magnetic nucleus, the SINGLE_ANISO procedure was used [11].

Results of calculations for anionic complex $\{(TMI\text{-}NPS)_2 \cdot Dy^{III}I_4\}^-$

As mentioned in the main text, structure of **1** contains two half and one whole independent unit $\{(TMI\text{-}NPS)_2 \cdot Dy^{III}I_4\}^-$, which differ slightly in geometry (e.g. most strongly in the dihedral angle between the planar fragments of TMI-NPS). Therefore, we performed electronic structure calculations for all three geometries of the anion complex $\{(TMI\text{-}NPS)_2 \cdot Dy^{III}I_4\}^-$. First, the calculations were performed using the SA-CASSCF(9,7) method for 21 sextets, 128 quartets, and 130 doublets, then spin-orbit coupling (SOC) was taken into account using quasi-degenerate perturbation theory (QDPT). As a result, the energies and wave-functions of 456 Kramers doublets were calculated, although only the 8 lowest energy Kramers doublets are important for analyzing the magnetic properties of the studied complexes (Fig. S11). To improve the accuracy of the calculations, the energies of all multiplets were recalculated at the NEVPT2 level and used in the subsequent SOC accounting. In addition, for one of the complexes, namely Dy3, the energy levels and wave-functions of Kramers doublets were also calculated using CASSCF(9,7)/SO-RASSI approach implemented in the OpenMolcas software suit. Figure S11 shows that at all levels of theory

the three Dy complexes have very close relative Kramers doublet (KD) energies, especially the energies of the first and second KDs. It should be also noted that the calculations at the CASPT2 level give results very close to that of simple CASSCF calculations, which may indicate a high accuracy of the calculated energies.

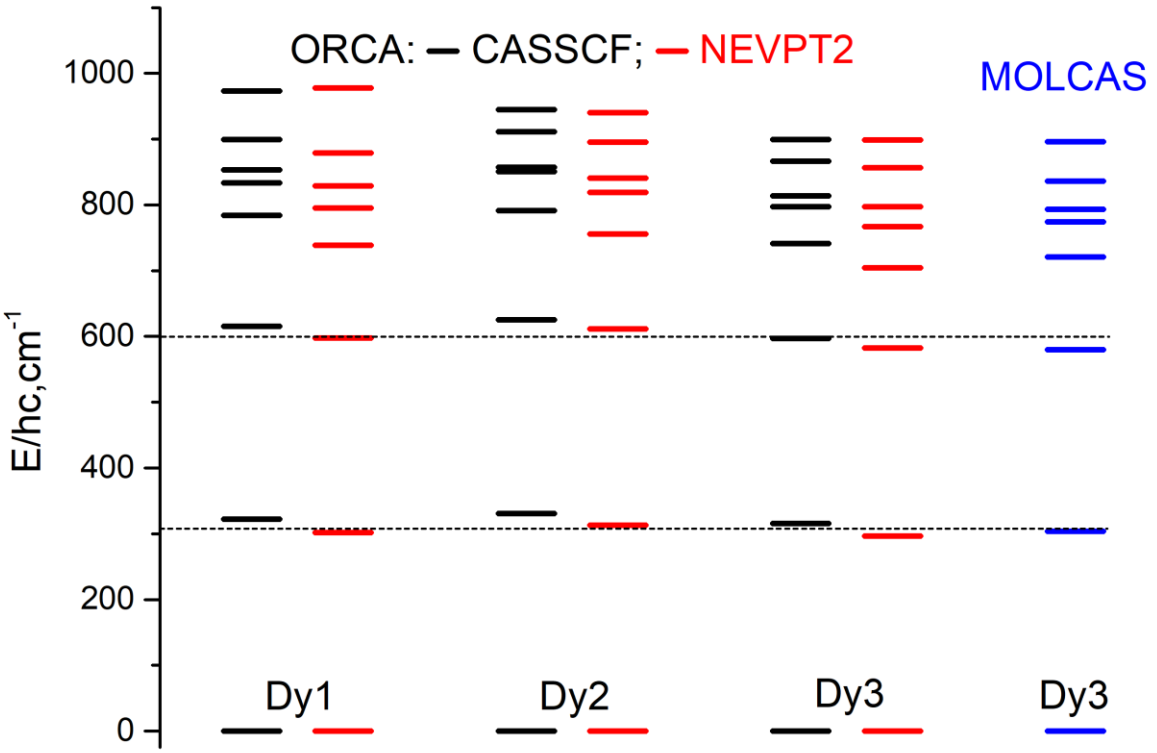

Fig. S10. Relative energies of *Kramers* doublets arising from the $^{6}H_{15/2}$ ground multiplet of the Dy ion in the ligand field. The energies were calculated at different level of theory: CASSCF(9,7)/SOC-QDPT (black bars) and CASSCF(9,7)/NEVPT2/SOC-QDPT (red bars) for three different anion complexes existing in the structure of **1**. For the Dy3 complex, calculations were also performed at CASSCF(9,7)/SO-RASSI level (blue bars) using the OpenMolcas software.

Using the SINGLE_ANISO procedure and described above results of ab initio calculations, we calculated a series of magnetic properties for complexes Dy1 – Dy3. Thus, the temperature dependences of the molar magnetic susceptibility (χ_M) and the product $\chi_M T$ were calculated for all types of complexes and at different magnetic fields, as well as in zero-field limit (Fig. S12). The predicted temperature dependences are found to be almost identical for the Dy1 – Dy3 complexes; they are also almost independent of the level of calculations.

At low temperature (T → 0) and low magnetic field (H → 0), the $\chi_M T$ values are predicted to reach 12.35 $cm^3 \cdot K \cdot mol^{-1}$. However, in a field of 1000 Oe, a drop in the $\chi_M T$ value is observed at T<10 K in agreement with experiment (Fig. 3a, main text). At 300 K, the $\chi_M T$ values reach 13.71 $cm^3 \cdot K \cdot mol^{-1}$, which is noticeably lower that the theoretical value for Dy^{III} ion (14.17 $cm^3 \cdot K \cdot mol^{-1}$, $^6H_{15/2}$, g = 4/3). This discrepancy is due to the significant energy splitting in the ligand field, especially of two lowest excited KDs ($\Delta E \approx 600$ cm^{-1}, Fig. S11).

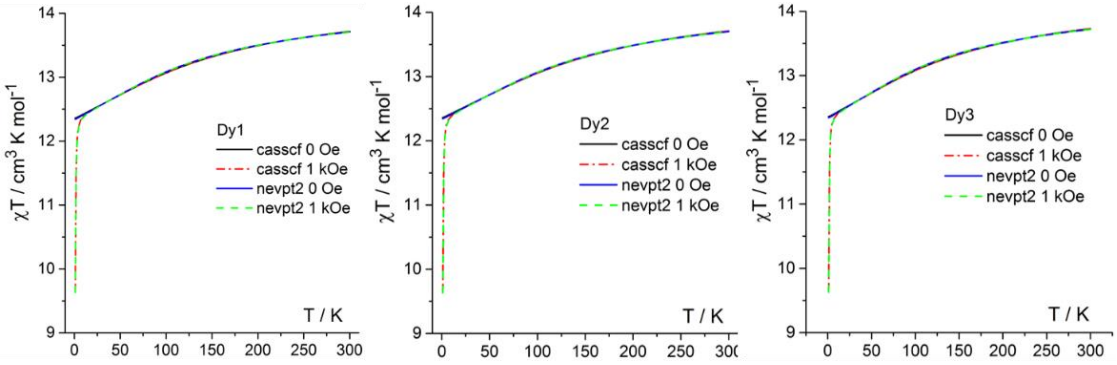

Fig. S11. Theoretical temperature dependences of the molar magnetic susceptibility (χ_M) as a product $\chi_M T$ predicted at different levels of theory (CASSCF(9,7)/SO-QDPT and CASSCF(9,7)/NEVPT2/SO-QDPT) for three types of Dy complexes existing in the unit cell and for different magnetic fields in the measurements.

We calculated also the decomposition of the KDs wave-functions on the components with definite J_z, where z is the easy axis for the ground Kramers doublet (KD1). As expected, the easy axes for KD1 of dysprosium complexes closely align with the O-Dy-O line (Fig. S13), although a slight deviation from this direction is clearly visible. Table S2 shows that the composition of the wave-functions of the KDs, as well as their energies, are almost independent on the level of calculation. Comparison of the results of Table S2 and S3 demonstrate also that this composition is almost the same for the three types of complexes presented in structure of **1**. It should be noted that for all complexes the lowest KDs (KD1 – KD3) have wave-functions corresponding to the almost pure states with J_z = 15/2, 13/2 and 11/2, which indicates the high oxyality of the complex $\{(TMI\text{-}NPS)_2 \cdot Dy^{III}I_4\}^-$.

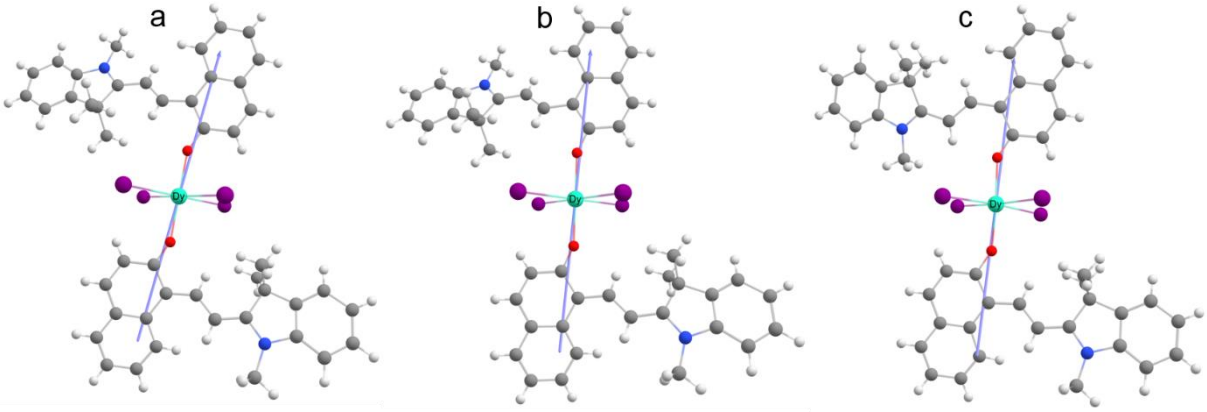

Figure S12. Crystal structures of Dy1 (a), Dy2 (b) and Dy3 (c) complexes with their easy axes for the ground Kramers doublets (KD1) shown as blue arrows.

Table S2. Decomposition of the wave-functions (CASSCF and NEVPT2 based) of the components of each KD of the Dy1 complex into wave-functions with definite J_z (z is the easy axis for KD1).

CASSCF based calcualtions			NEVPT2 based calculations		
KD	ΔE, cm^{-1}	$\|J_z\|$ (contribution in %)	KD	ΔE, cm^{-1}	$\|J_z\|$ (contribution in %)
1	0	**15/2 (99.9)**	1	0	**15/2 (100.0)**
2	322.2	**13/2 (99.1)**	2	302.0	**13/2 (99.1)**
3	615.4	**11/2 (94.4)**, 9/2 (2.7), 3/2 (2.1)	3	597.8	**11/2 (93.4),** 9/2 (3.1), 3/2 (2.7)
4	784.2	**1/2 (55.1)**, 9/2 (32.8), 7/2 (6.9), 3/2 (3.5)	4	738.4	**1/2 (75.1)**, 9/2 (12.9), 3/2 (5.7), 7/2 (4.5)
5	833.2	**3/2 (36.0)**, 9/2 (23.9), 1/2 (13.6), 5/2 (13.2), 7/2 (11.1), 11/2 (2.1)	5	795.2	**3/2 (57.3**), 5/2 (19.5), 9/2 (9.8), 7/2 (8.6), 11/2 (2.7), 1/2 (1.9)
6	853.1	**3/2 (32.4)**, 9/2 (27.1), 1/2 (17.5), 5/2 (17.0), 7/2 (5.3)	6	829.0	**9/2 (55.7)**, 1/2 (12.7), 3/2 (11.9), 7/2 (10.4), 5/2 (8.0)
7	899.1	**5/2 (36.8)**, 7/2 (30.7), 3/2 (17.3), 1/2 (9.1), 9/2 (5.3)	7	879.1	**5/2 (43.7)**, 7/2 (25.9), 3/2 (15.6), 9/2 (7.2), 1/2 (6.7)
8	973.3	**7/2 (45.9)**, 5/2 (32.0), 3/2 (8.7), 9/2 (8.4), 1/2 (4.6)	8	977.9	**7/2 (50.5)**, 5/2 (27.5), 9.2 (11.2), 3/2 (6.8), 1/2 (3.6)

Table S3. Decomposition of the wave-functions of the components of each KD of the Dy2 and Dy3 complex into wave-functions with definite J_z at different levels of calculations

Complex Dy2 (NEVPT2, ORCA)			Complex Dy3 (CASSCF, MOLCAS)		
KD	ΔE, cm^{-1}	$\|J_z\|$ (contribution in %)	KD	ΔE, cm^{-1}	$\|J_z\|$ (contribution in %)
1	**0**	**15/2 (99.9)**	1	**0**	**15/2 (99.9)**
2	313.4	**13/2 (99.3)**	2	296.4	**13/2 (99.4)**
3	611.2	**11/2 (95.0)**, 3/2 (2.6), 9/2 (1.8)	3	582.5	**11/2 (94.6),** 3/2 (3.6)
4	755.9	**1/2 (76.1)**, 9/2 (15.9), 7/2 (4.1), 3/2 (2.3)	4	704.2	**1/2 (78.9)**, 9/2 (12.2), 3/2 (3.6), 7/2 (2.9), 5/2 (1.7)
5	818.7	**3/2 (76.8)**, 5/2 (15.3), 9/2 (3.2), 11/2 (2.3), 1/2 (1.7)	5	767.0	**3/2 (70.0)**, 5/2 (12.2), 7/2 (6.8), 9/2 (4.9), 1/2 (3.6), 11/2 (2.5)
6	840.7	**9/2 (66.9)**, 1/2 (17.1), 7/2 (11.3), 5/2 (2.0)	6	797.3	**9/2 (64.3)**, 5/2 (13.0), 3/2 (10.0), 1/2 (9.3), 7/2 (2.2)
7	895.0	**5/2 (60.0)**, 3/2 (15.4), 7/2 (15.1), 9/2 (6.7), 1/2 (2.3)	7	856.5	**5/2 (54.8)**, 7/2 (27.3), 9/2 (9.2), 3/2 (5.6), 1/2 (2.7)
8	939.9	**7/2 (68.5)**, 5/2 (21.4), 9/2 (5.6), 1/2 (2.8), 3/2 (1.6)	8	898.7	**7/2 (60.5**), 5/2 (17.9), 9.2 (8.0), 3/2 (7.3), 1/2 (5.5)

Using the SINGLE_ANISO procedure and the results of *ab initio* calculations, we have also calculated the g-tensor components for the lowest KDs (states with pseudo-spin $\tilde{S} = 1/2$) of three types of dysprosium complexes. Note that for perfectly anisotropic Dy^{III} complexes (e.g., linear complexes with halogen anions),[12] the g-tensor components in the ground state (KD1) are g_z = 20.0, g_x = g_y = 0. Tables S4 and S5 show that the magnetic properties of the three types of Dy complexes are again very close. Moreover, the g_z component for all Dy complexes (19.85 – 19.86) is close to 20 and the transversal components are negligibly small (10^{-5} – 10^{-4}), these values are in good agreement with the zero-field SIM behavior for compound **1**.

Table S4. Principal values of the g-tensors for the lowest energy KDs in Dy1 complex calculated at different levels of theory.

CASSCF based				NEVPT2 based			
KD	g_x	g_y	g_z	KD	g_x	g_y	g_z
1	**3×10^{-5}**	**6×10^{-5}**	**19.863**	1	**2×10^{-5}**	**9×10^{-5}**	**19.849**
2	0.006	0.007	17.058	2	0.010	0.011	17.064
3	0.037	0.066	14.151	3	0.087	0.149	14.083
4	9.504	7.358	3.538	4	2.156	7.055	12.279
5	0.982	1.508	11.696	5	1.216	4.154	10.489
6	7.941	6.781	2.236	6	1.134	4.421	8.659
7	3.355	6.504	10.282	7	9.364	6.820	3.255
8	0.073	0.280	17.831	8	0.139	0.335	17.746

Table S5. Components of the g-tensors for the lowest energy KDs of Dy2 and Dy3 complex calculated using results of NEVPT2 based calculationas.

Dy2 complex				Dy3 complex			
KD	g_x	g_y	g_z	KD	g_x	g_y	g_z
1	**6×10^{-5}**	**1.2×10^{-4}**	**19.850**	1	**5×10^{-5}**	**1.4×10^{-4}**	**19.849**
2	0.011	0.012	17.053	2	0.015	0.016	17.048
3	0.051	0.122	14.070	3	0.223	0.337	13.925
4	11.798	7.653	2.619	4	2.205	6.718	13.088
5	1.938	5.059	9.334	5	1.195	3.140	11.624
6	0.194	1.439	10.355	6	0.447	4.377	8.968
7	7.439	5.969	3.883	7	0.152	5.223	12.058
8	0.734	0.860	14.580	8	1.328	2.692	15.880

Table S6. Angles between the easy axes of excited Kramers doublets and the easy axis of the ground Kramer doublet (KD1) calculated for Dy1 – Dy3 complexes.

Complex	KDs	1	2	3	4	5	6	7	8
Dy1	∠, °	0	3.8	8.2	89.6	71.1	41.5	72.6	63.6
Dy2	∠, °	0	3.1	6.2	96.1	78.6	30.1	93.3	55.4
Dy3	∠, °	0	2.6	4.2	89	75.7	20.4	68.5	66.2

Finally, for all Dy complexes (Dy1 – Dy3), the magnetization blocking barriers and the corresponding matrix elements of the magnetic transition moments were calculated (Fig. S14 – S15).

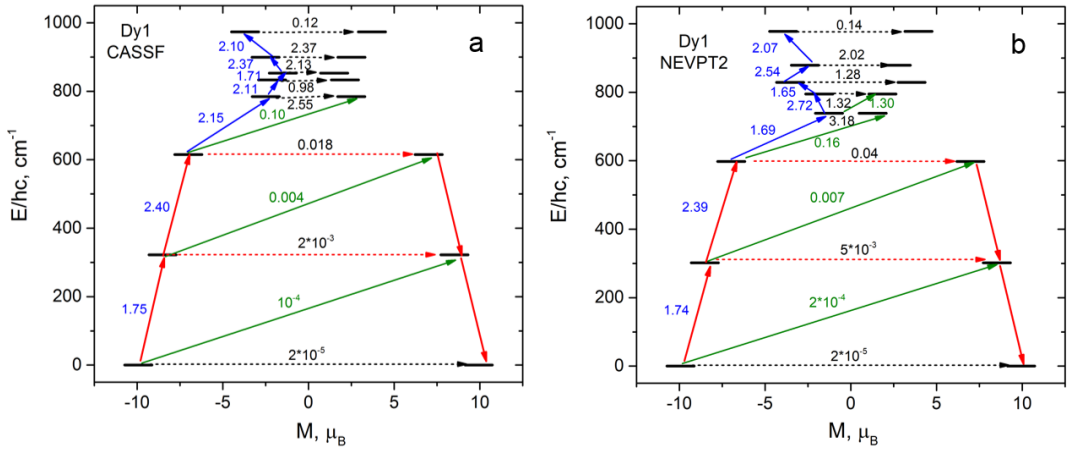

Fig. S13. The magnetization blocking barrier for the Dy1 complex. The thick black bars represent the Kramers doublets as a function of their magnetic moments. The dashed lines correspond to quantum tunneling of magnetization (QTM); the red and blue lines represent Orbach relaxation processes; the green lines show possible Orbach processes. The numbers next to each arrow stand for the mean absolute values of the corresponding matrix elements of transition magnetic moment $((|\mu_x| + |\mu_y| + |\mu_z|)/3)$. The path shown by red arrows represents the most probable magnetic relaxation paths in the Dy1 complex. The presented results correspond to the CASSCF (a) and CASSCF/NEVPT2 (b) based calculations.

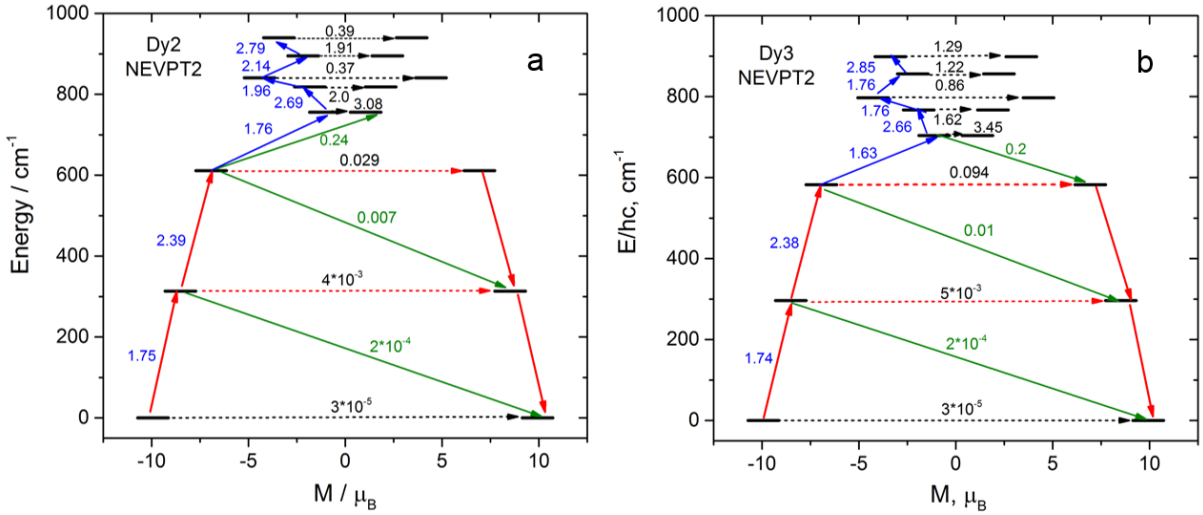

Fig. S14. The magnetization blocking barrier for the Dy2 (a) and Dy3 (b) complexes. The presented results correspond to the CASSCF/NEVPT2 based calculations. All other details are the same as in Fig. S14.

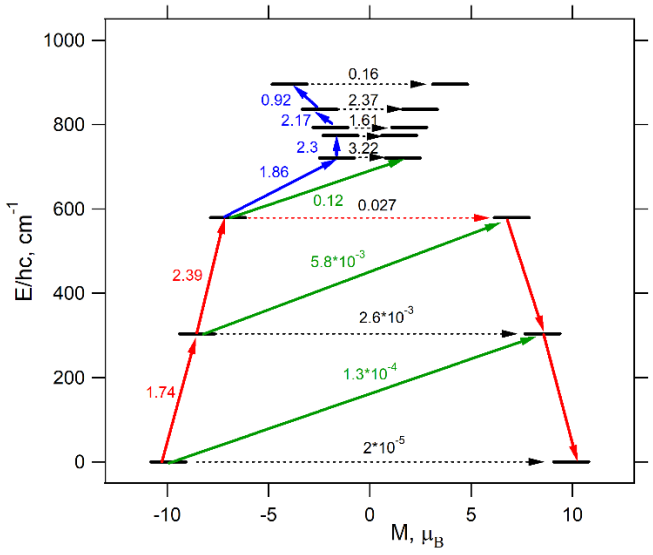

Fig. S15. The magnetization blocking barrier in the Dy3 complex, calculated at the CASSCF/SO-RASSI level using MOLCAS program. All other details are the same as in Fig. S13.

Complex 2.

Static experimental magnetic properties

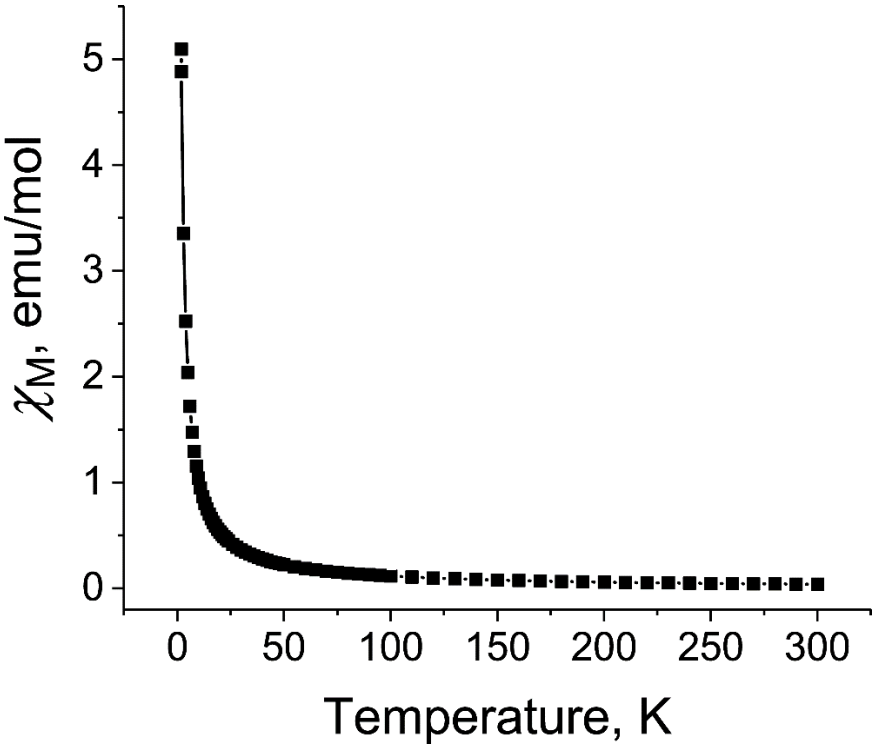

Fig. S16. Data of SQUID measurements for polycrystalline **2**. The temperature dependence of molar magnetic susceptibility is shown in the 1.9-300 K range after the subtraction of a temperature independent contribution.

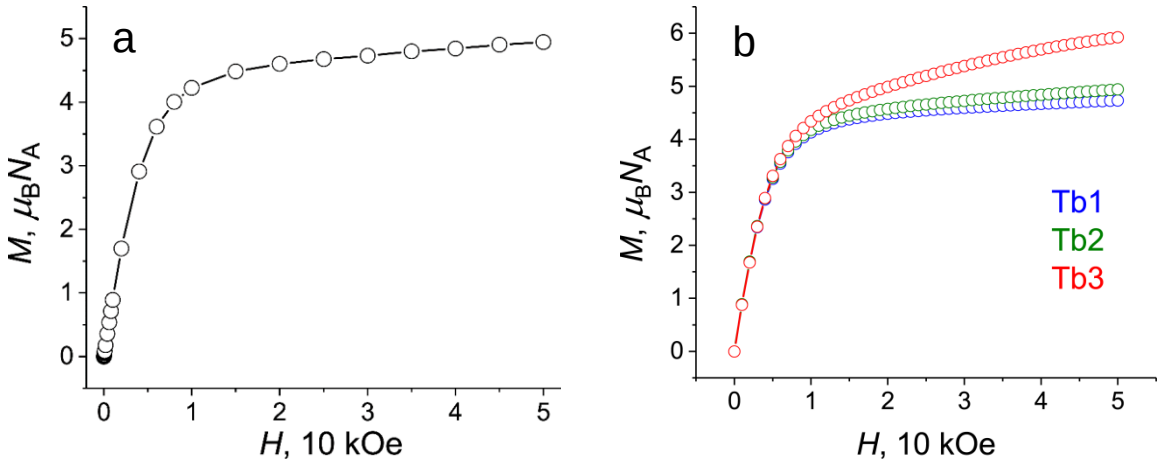

Fig. S17. Field-dependent magnetization for polycrystalline **2** at 2 K; (b) High-field powder magnetization at 2 K calculated for three structurally different Tb complexes (Tb1-Tb3) using SINGLE-ANISO procedure and results of the SA-CASSCF(8,7)/NEVPT2/SOC-QDPT calculations.

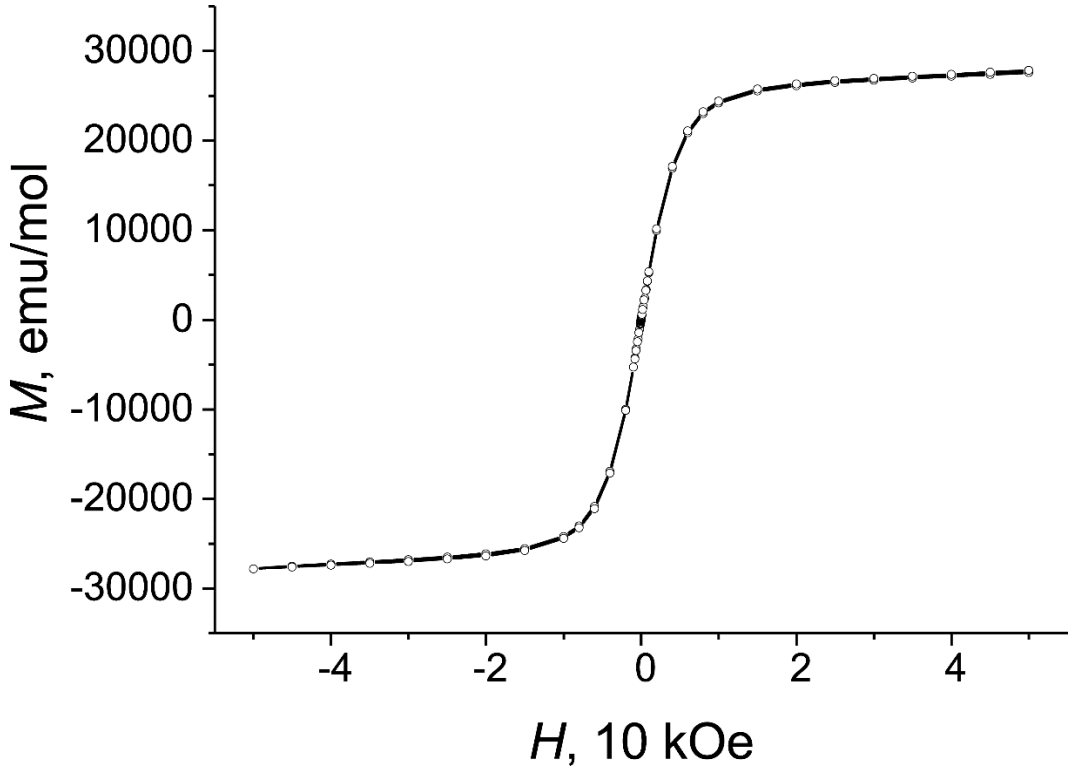

Fig. S18. Hysteresis loops for polycrystalline **2** at 2 K.

Experimental dynamic magnetic properties of 2.

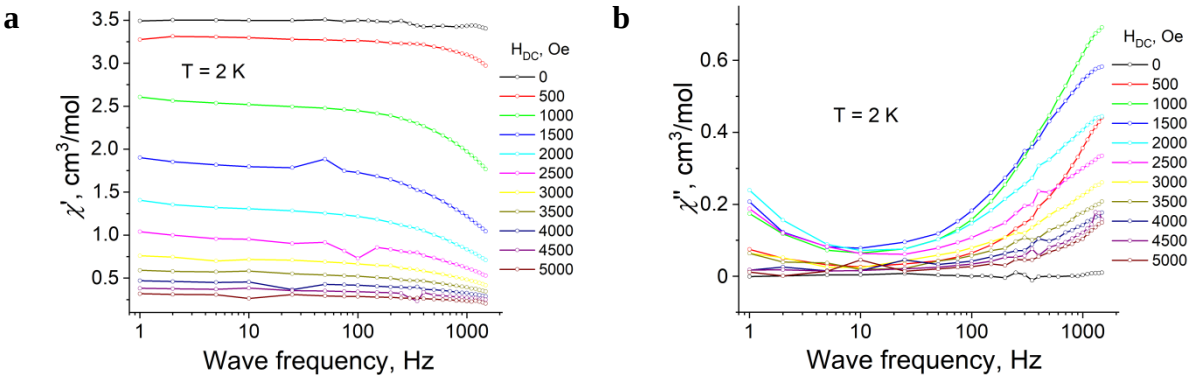

Fig. S19. Frequency dependences of in-phase (χ') (a) and out-of-phase (χ'') (b) AC susceptibility for **2** at different applied static magnetic fields H_{DC} from 0 to 1000 Oe.

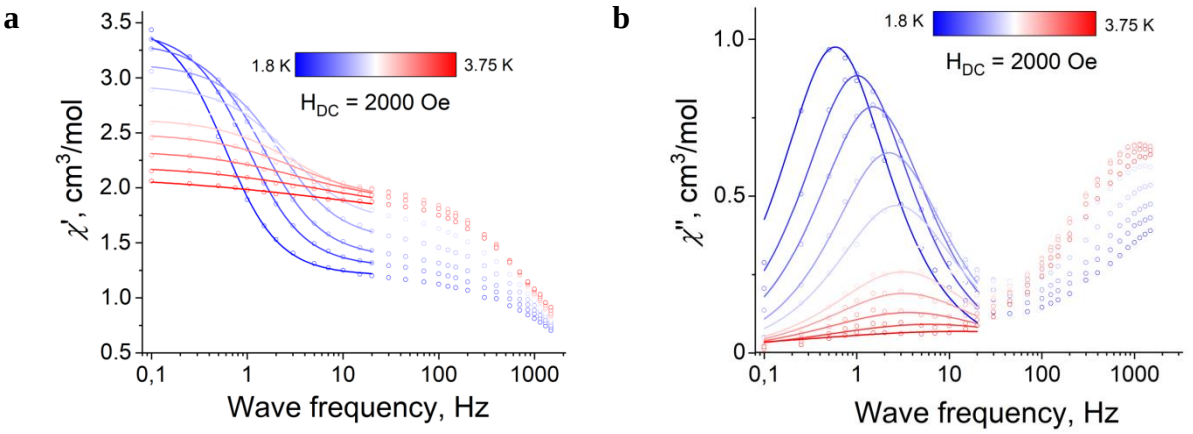

Fig. S20. Frequency dependences of in-phase (χ') (a) and out-of-phase (χ'') (b) AC magnetic susceptibilities for **2** in 2000 Oe static magnetic field and temperatures of 1.8 – 3.75 K. Solid lines represent the fitting of the data by the generalized Debye model.

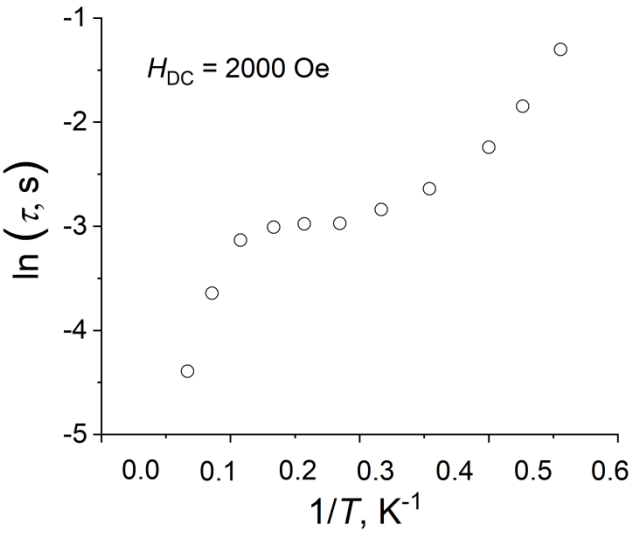

Fig. S21. SQUID measurement data for polycrystalline samples of salt **2**. Dependence of the relaxation time $ln(\tau)$ on the reciprocal temperature measured in a 2000 Oe magnetic field.

Results of model calculations for anionic complex $\{(TMI\text{-}NPS)'_2{\cdot}Tb^{III}I_4\}^-$

First, three different calculation approaches were tried for the Tb complex with a geometry almost identical to that of Tb3 (instead of the –CH=CH– group in the ligands of Tb3, there is the –N=CH– group in Tb3′). SA-CASSCF(8,7) calculations were first performed for 7 septets, 140 quintets, 588 triplets and 490 singlets, all possible multiplets that arise from the f^8 electronic configuration. Then spin-orbit coupling (SOC) was taken into account using quasi-degenerate perturbation theory (QDPT) implemented in the ORCA software suit (1st approach) or SOC was taken into account using the SO-RASSI procedure implemented in the OpenMolcas software package (2nd approach). As a result, the energies and wave-functions of 3003 non-degenerate spin-orbit states were calculated, although only the 13 lowest energy levels arising from the $^7F_6$ state of the Tb^{3+} cation under the action of the ligand field are important for analyzing the magnetic properties of the studied complexes (Fig. S22). Since these calculations are tremendously time and resource consuming, we also tested a third, much less laborious approach in which SA-CASSCF(8,7) calculations were performed for 7 septets and 5 quintets. In addition, the energy levels and wave-functions of spin-orbit states of Tb3′ complex were also calculated using CASSCF(8,7)/SO-RASSI approach implemented in the OpenMolcas software suit. Fig. S22 shows that all approaches yield close energies of spin-orbit states and similar values of tunnel splitting (Δ_{tun}) of quasi-degenerate non-Kramers doublets (Fig. S22).

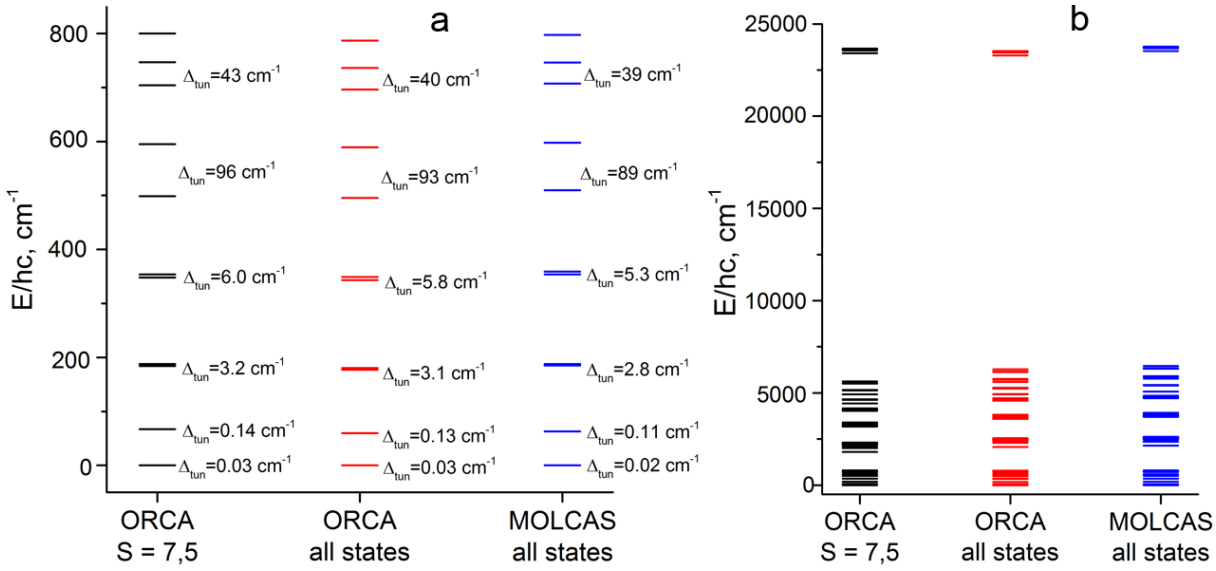

Fig. S22. Relative energies of spin-orbit states of the Tb3′ complex calculated at different levels of theory: CASSCF(8,7)/SOC-QDPT considering 7 septets and 5 quintets in SA-CASSCF(8,7) calculations (black bars) or 7 septets, 140 quintets, 588 triplets and 490 singlets (red bars), and at the CASSCF(8,7)/SO-RASSI level considering 7 septets, 140 quintets, 588 triplets and 490 singlets (blue bars). a) Spin-orbit states arising from the $^7F_6$ ground multiplet of the Tb^{3+} ion in the ligand field and the tunnel splitting values (Δ_{tun}) of the quasi-degenerate non-Kramers doublets.

To improve the accuracy of the calculations, the energies of all multiplets were recalculated at the NEVPT2 level and used in the subsequent SOC accounting. Fig. S23 shows the spin-orbit energy levels calculated considering 7 septets, 140 quintets, 588 triplets and 490 singlets. It is seen that full splitting of the ground $^7F_6$ term is practically the same in calculations based on the CASSCF and NEVPT2 procedures (787 and 791 cm^{-1}, respectively). However, the energies of the lowest four quasi-degenerate non-Kramers doublets are greatly reduced at the NEVPT2 level, especially the energy of the first excited non-Kramers doublet (by about 13.9 times).

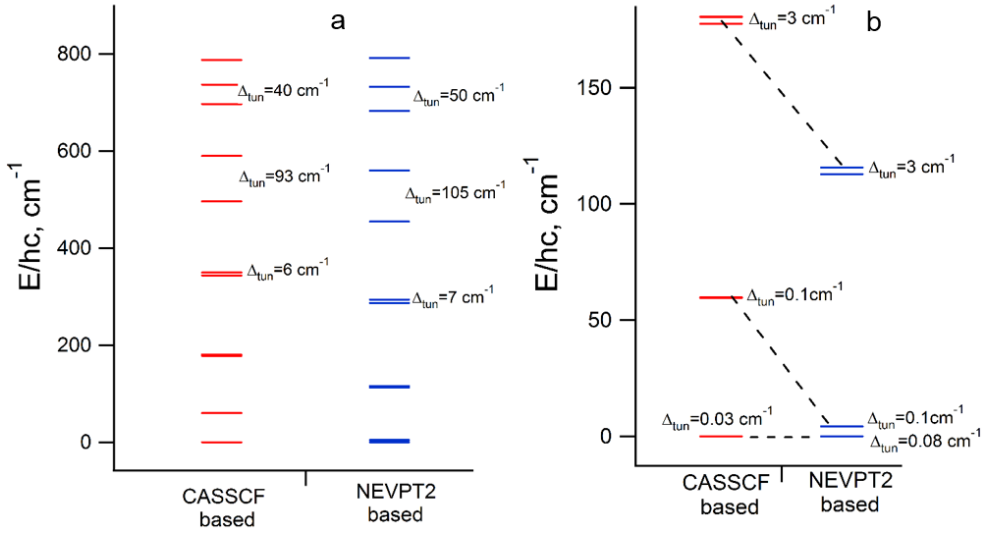

Fig. S23. a) Relative energies of spin-orbit states of the Tb3′ complex arising from the $^7F_6$ ground multiplet of the Tb^{3+} ion and the tunnel splitting values (Δ_{tun}) of the quasi-degenerate non-Kramers doublets. Calculations were performed at the CASSCF(8,7)/SOC-QDPT (red bars) and CASSCF(8,7)/NEVPT2/SOC-QDPT (blue bars) levels, taking into account 7 septets, 140 quintets, 588 triplets and 490 singlets in the SA-CASSCF(8,7) calculations. b) Relative energies and tunnel splitting values (Δ_{tun}) for the three lowest non-Kramers doublets.

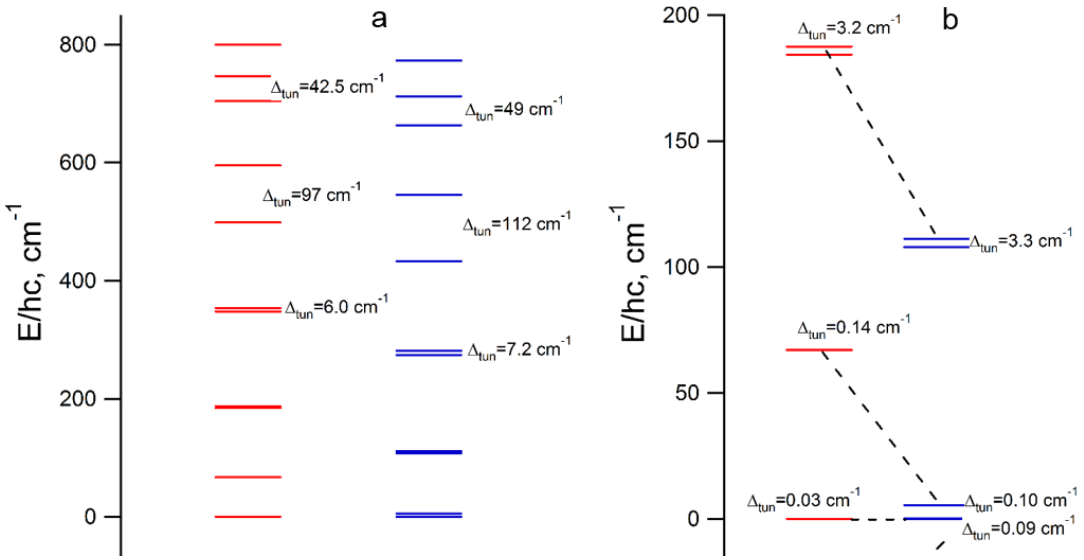

Fig. S24. a) Relative energies of spin-orbit states of the Tb3′ complex arising from the $^7F_6$ ground multiplet of the Tb^{3+} ion and the tunnel splitting values (Δ_{tun}) of the quasi-degenerate non-Kramers doublets. Calculations were performed at the CASSCF(8,7)/SOC-QDPT (red bars) and CASSCF(8,7)/NEVPT2/SOC-QDPT (blue bars) levels considering 7 septets and 5 quintets in the SA-CASSCF(8,7) calculations. b) Relative energies and tunnel splitting values (Δ_{tun}) for the three lowest non-Kramers doublets.

A completely similar situation is observed in the case of calculations considering only 7 septets and 5 quintets (Fig. S24): namely, the total splitting of the ground $^7F_6$ term of the Tb^{3+} cation is almost identical in calculations using CASSCF and CASSCF/NEVPT2 procedures (799.9 and 773 cm^{-1}, respectively). At the same time, the relative energies of the lowest excited quasi-degenerate non-Kramers doublets are strongly reduced at the NEVPT2 level, compared to the CASSCF. For example, the relative energy of the first excited non-Kramers doublet is reduced by a factor of 12.2. Thus, the results based on CASSCF(8,7) and CASSCF(8,7)/NEVPT2 procedures are close for cases where both a very large number of spin multiplets (1225) and only 12 spin multiplets (7 septets and 5 quintets) are considered. The use of computer resources in the case of the second type calculations is tremendously reduced. Therefore, all further calculations for three types of Tb complexes (Tb1 – Tb3) were carried out taking into account 12 spin-multiplets.

It should be recalled that in the case of Dy complexes (Dy1 – Dy3), all calculation results based on both CASSCF(9,7) and CASSCF(9,7)/NEVPT2 were very close to each other (Figs S11, S12, S14 and Tables S2 and S4). This may be an indication of the high accuracy of these calculations and the closeness of the theoretical predictions for studied Dy complexes to the experiment. In contrast to the Dy complexes discussed above, in the case of the Tb3′ complex the difference of the results obtained based of the CASSCF and NEVPT2 calculation is very significant. In principle, this may indicate that the application of the second-order multi-reference perturbation theory may not be sufficient to obtain very accurate results consistent with experiment.

Results of calculations for anionic complex $\{(TMI\text{-}NPS)_2 \cdot Tb^{III}I_4\}^-$

As mentioned in the main text, structure of **2** contains two half and one whole independent unit $\{(TMI\text{-}NPS)_2 \cdot Tb^{III}I_4\}^-$, which differ slightly in geometry (e.g. most strongly in the dihedral angle between the planar fragments of TMI-NPS). Therefore, we performed electronic structure calculations for all three geometries of the anionic complex $\{(TMI\text{-}NPS)_2 \cdot Tb^{III}I_4\}^-$. First, the calculations were performed using the SA-CASSCF(8,7) method for 7 septets, 5 quintets, then the spin-orbit coupling (SOC) was taken into account using quasi-degenerate perturbation theory (QDPT). The basis set SARC2-DKH-QZVP was used for Tb, SARC2-DKH-TZVP for atom I, and DKH-def2-tzvp(-f) for all other atoms. As a result, the energies and wave-functions of 74 states were calculated, although only 13 with the lowest energy, arising from the splitting in the ligand field of the ground $^7F_6$ term of the Tb^{3+} cation, are important for analyzing the magnetic properties of the studied complexes (Fig. S24). To account for dynamic electron correlation and to improve the accuracy of calculations, the energies of the spin multiplets were recalculated at the NEVPT2 level and used in the subsequent SOC accounting using QDPT.

Figure S24 shows that, as for compound **1**, the total splitting of the ground term is practically independent of the calculation level, but slightly decreases (by about 11%) in the Tb1 – Tb3 series. As in the case of model complex Tb3′, the energies of the lowest excited states (non-Kramers doublets) are significantly reduced in the calculations based on the NEVPT2 level (Fig. S25b). Moreover, at both levels of theory, a significant energy decrease is observed for Tb complexes in the Tb1 – Tb3 series. Thus, at the highest level of theory, the energy of the first excited non-Kramers double is 72 cm^{-1} for Tb1, 36 cm^{-1} for Tb2, and only 7.5 cm^{-1} for the Tb3 complex.

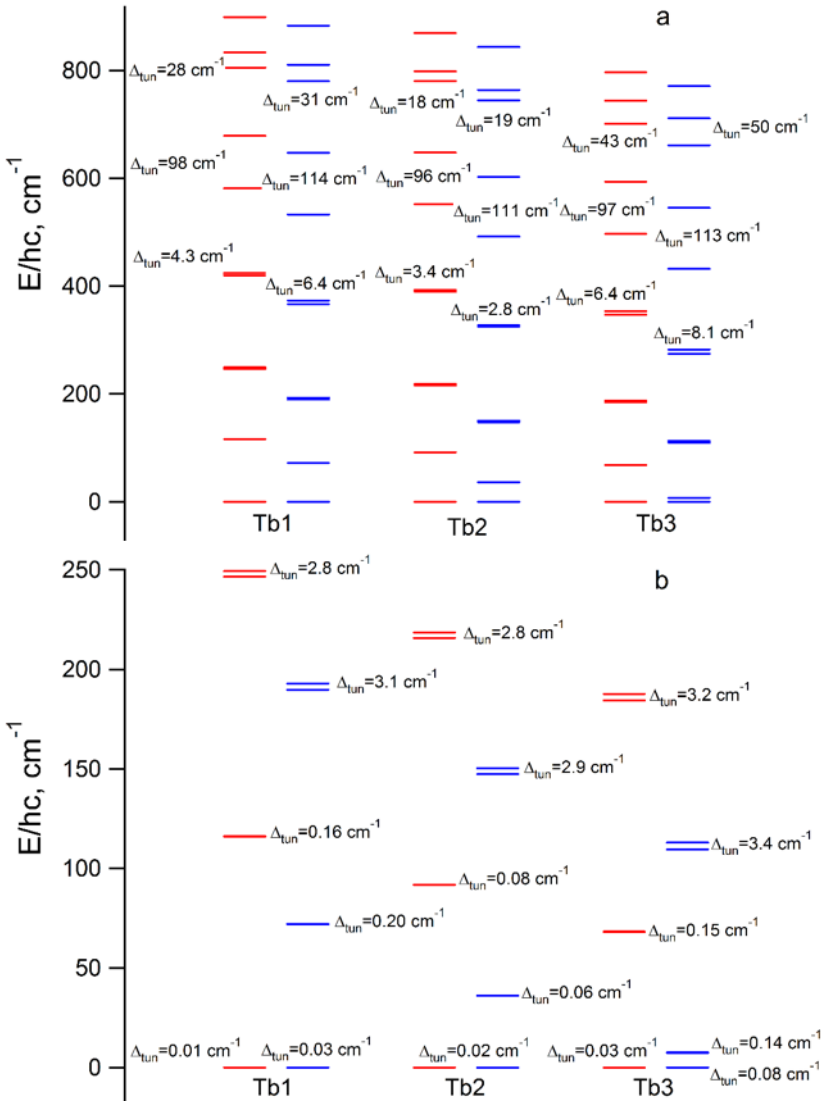

Fig. S25. Relative energies of non-degenerate states arising from the $^7F_6$ ground term of the Tb^{3+} cation in the ligand fields of complexes Tb1, Tb2 and Tb3; the tunnel splitting values (Δ_{tun}) are also presented for the highest (a) and lowest (b) quasi-degenerate non-Kramers doublets. The energies were calculated at different level of theory: CASSCF(8,7)/SOC-QDPT (red bars) and CASSCF(8,7)/NEVPT2/SOC-QDPT (blue bars) for three different anion complexes existing in the structure of **2**.

Using the SINGLE_ANISO procedure and the results of ab initio calculations described above, we calculated a number of magnetic properties for complexes Tb1 – Tb3. Thus, the temperature dependences of the molar magnetic susceptibility (χ_M) and the product $\chi_M T$ in the experimental magnetic fields (1000 Oe) as well as in the zero-field were calculated for all types of complexes Tb1 – Tb3 (Fig. S26). The predicted temperature dependences for the Tb1

– Tb3 complexes are slightly different and also strongly dependent on the level of calculations (CASSCF and NEVPT2). At low temperature (T → 0) and low magnetic field (H → 0), the $\chi_M T$ values reach 10.07 – 10.12 $cm^3 \cdot K \cdot mol^{-1}$ for all cases except the NEVPT2-based calculations for Tb3 (9.7 $cm^3 \cdot K \cdot mol^{-1}$). Indeed, at low T and H, the value of $\chi_M T$ for SIMs is close to the value of $\frac{g_{eff,z}^2}{32} \approx 10.12$ $cm^3 \cdot K \cdot mol^{-1}$.[13] However, in the 1000 Oe field, a drop in the $\chi_M T$ value is observed at T<10 K in agreement with experiment (Fig. 5a, main text). At 300 K, the $\chi_M T$ values reach 11.69 – 11.72 $cm^3 \cdot K \cdot mol^{-1}$, which is close to the theoretical value for Tb^{III} ion (11.82 $cm^3 \cdot K \cdot mol^{-1}$, $^7F_6$, $g_J = 3/2$).

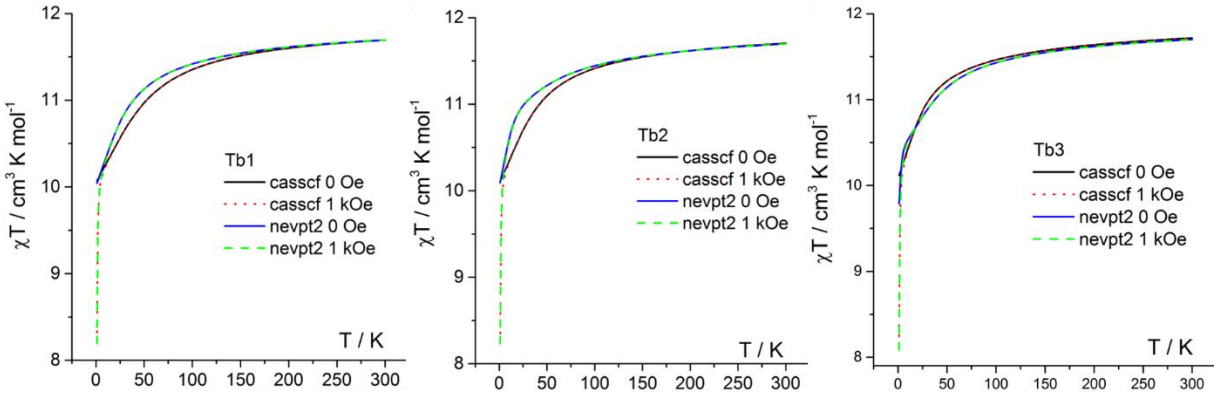

Fig. S26. Theoretical temperature dependences of the molar magnetic susceptibility (χ_M) as a product $\chi_M T$ predicted at different levels of theory (SA-CASSCF(8,7)/SO-QDPT and SA-CASSCF(8,7)/NEVPT2/SO-QDPT) for three types of Tb complexes existing in the unit cell of 2 and for low (H → 0 Oe) and high (H = 1000 Oe) magnetic fields in the measurements.

Using the SINGLE_ANISO procedure and the results of the CASSCF(8,7)/NEVPT2/SO-QDPT calculations described above, the g_z components for the lowest non-Kramers doublets were also calculated for three types of Tb complexes. Moreover, a decomposition of the wave-functions into components with a certain J_z (where z is the easy axis for the ground non-Kramers doublet) was performed.

Table S7. Decomposition of the wave-functions of the components of the non-Kramers doublets of the Tb1 complex calculated at the CASSCF(8,7)/NEVPT2/SOC-QDPT level into wave-functions with a certain J_z (z is the easy axis for the ground state non-Kramers doublet).

Complex	Energy level	E, cm^{-1}	g_z	$\|J_z\|$ (contribution in %)
Tb1 $^7F_6$	E_1	0	17.88	**6 (98.6)**
	E_2	0.026		**6 (98.6)**
	E_3	71.9	15.47	**5 (88.8)**, 4 (10.8)
	E_4	72.1		**5 (88.8)**, 4 (10.6)
	E_5	189.8	11.82	**4 (64.4)**, 3 (23.4)
	E_6	192.9		**4 (65)**, 3 (23)
	E_7	366.6	8.28	**3 (41.2)**, 2 (34), 4 (18.6)
	E_8	373		**3 (47.2)**, 2 (23.8), 4 (19.8)
	E_9	533	5.22	**1 (38.6**), 2 (27.2), 3 (25.2)
	E_{10}	647.3		**2 (31)**, 1 (27.4), 2 (26.4), 0 (11.8)
	E_{11}	780.1	2.17	**0 (50)**, 2 (22.2), 1 (17.6)
	E_{12}	810.8		**2 (41.2)**, 1 (35.4), 0 (20.2)
	E_{13}	883.1	–	–

Table S8. Decomposition of the wave-functions of the components of the non-Kramers doublets of the Tb2 complex calculated at the CASSCF(8,7)/NEVPT2/SOC-QDPT level into wave-functions with a certain J_z (z is the easy axis for the ground state non-Kramers doublet).

Complex	Energy level	E, cm^{-1}	g_z	$\|J_z\|$ (contribution in %)
Tb2 $^7F_6$	E_1	0	17.94	**6 (98.8)**
	E_2	0.022		**6 (98.9)**
	E_3	36.1	15.75	**5 (83.4)**, 4 (15.2)
	E_4	36.2		**5 (83.6)**, 4 (15.2)
	E_5	147.4	11.7	**4 (57.8)**, 3 (23.8), 5 (14.6)
	E_6	150.3		**4 (58.4)**, 3 (23.2), 5 (14.8)
	E_7	324.9	8.25	**3 (43.4)**, 2 (26.4), 4 (22.2)
	E_8	327.7		**3 (43)**, 2 (28.2), 4 (22.4)
	E_9	491.8	5.2	**1 (40.2)**, 2 (28.6), 3 (27.4)
	E_{10}	602.6		**2 (34.8)**, 3 (27.6), 1 (19), 0 (16)
	E_{11}	744.5	2.16	**1 (45.6**), 2 (31), 0 (14.2)
	E_{12}	763.8		**0 (54.1)**, 2 (33.2), 1 (11.2)
	E_{13}	843.3	–	–

Table S9. Decomposition of the wave-functions of the components of the non-Kramers doublets of the Tb3 complex calculated at the CASSCF(8,7)/NEVPT2/SOC-QDPT level into wave-functions with a certain J_z (z is the easy axis for the ground state non-Kramers doublet).

Complex	Energy level	E, cm^{-1}	g_z	$\|J_z\|$ (contribution in %)
Tb3 $^7F_6$	E_1 E_2	0 0.08	17.49	**|6> (92.4)** **|6> (92.8)**
	E_3 E_4	7.4 7.5	16.76	|5> (71), |4> (22.4) |5> (71.4), |4> (22.4)
	E_5 E_6	109.6 112.9	11.69	|4> (36), |3> (32), |5> (23.2) |4> (36.6), |3> (32.6), |5> (23.4)
	E_7 E_8	274.5 282.6	8.25	|2> (40.4), |4> (26.8), |3> (20.8) |4> (29.4), |3> (27.4), |2> (27.4)
	E_9 E_{10}	432 545.3	5.22	|1> (44.8), |3> (30), |2> (12) |3> (31.4), |1> (30.2), |0> (18.2), |2> (14.4)
	E_{11} E_{12}	661.3 711.4	2.19	|0> (63.4), |2> (22) |2> (45.6), |1> (39.8), |3> (10.6)
	E_{13}	771	–	–

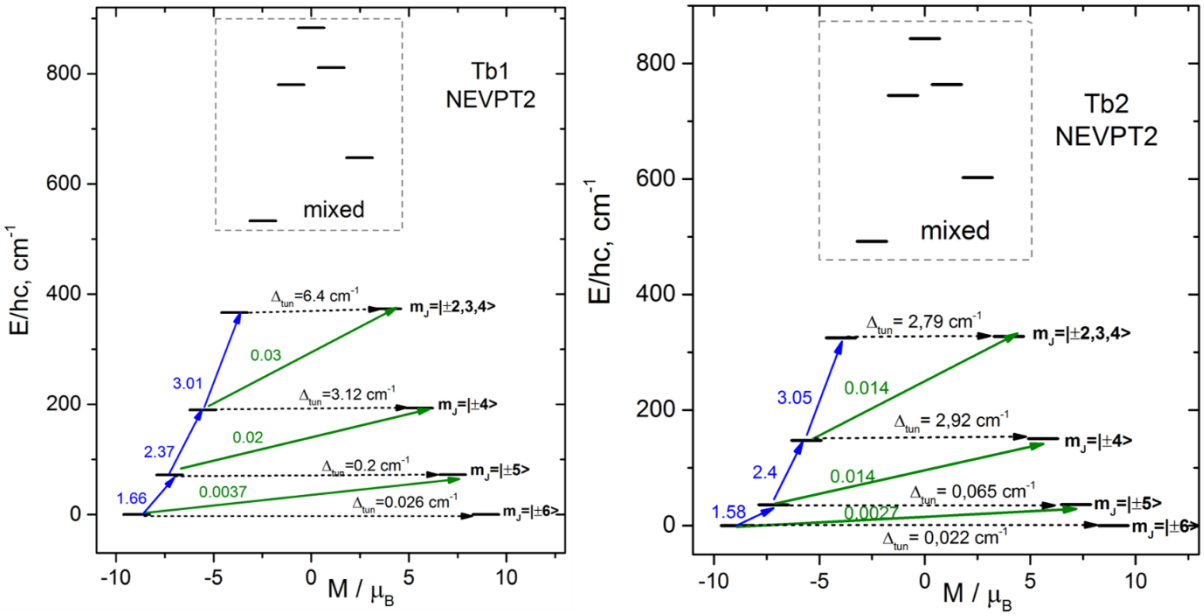

Fig. S27. The magnetization blocking barrier for the Tb1 (left) and Tb2 (right) complexes. The thick black bars represent the spin-orbit states as a function of their magnetic moments. The dashed lines correspond to quantum tunneling of magnetization (QTM); the blue lines represent Orbach relaxation processes; the green lines show possible Orbach processes. Blue and green numbers next to each arrow stand for the mean absolute values of the corresponding matrix elements of transition magnetic moment (($|\mu_x|$ + $|\mu_y|$ +$|\mu_z|$)/3). Black numbers denote the tunneling splitting of the components of the non-Kramers doublets. The presented results correspond to the CASSCF/NEVPT2-based calculations.

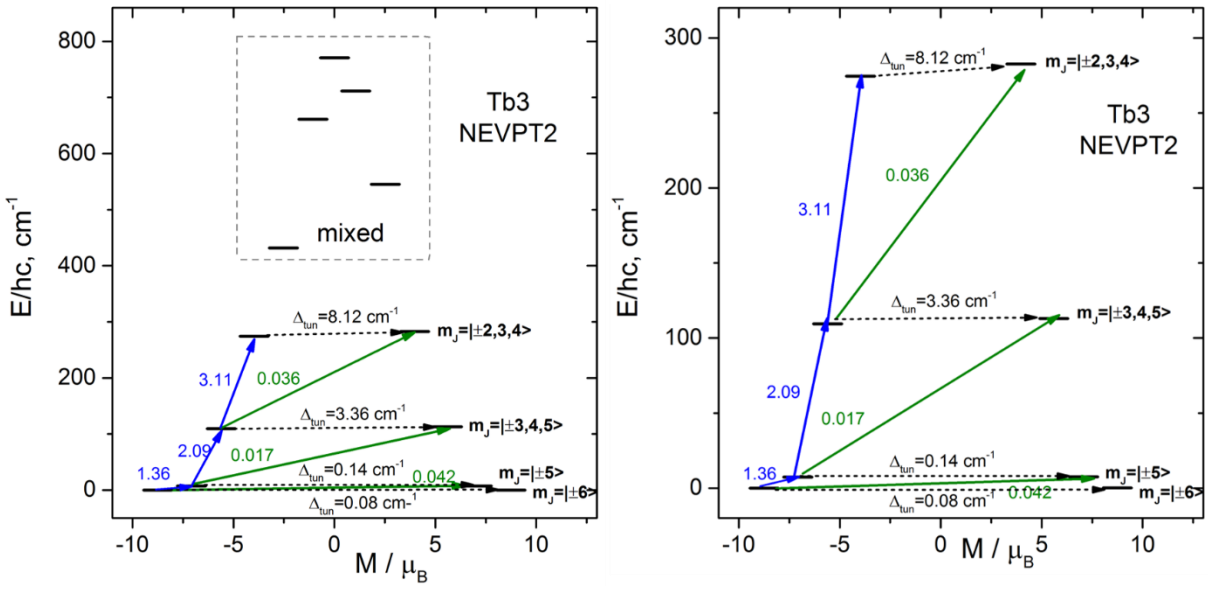

Fig. S28. The magnetization blocking barrier for the Tb3 complex. The thick black bars represent the spin-orbit states as a function of their magnetic moments. The dashed lines correspond to quantum tunneling of magnetization (QTM); the blue lines represent Orbach relaxation processes; the green lines show possible Orbach processes. Blue and green numbers next to each arrow stand for the mean absolute values of the corresponding matrix elements of transition magnetic moment (($|\mu_x|$ + $|\mu_y|$ +$|\mu_z|$)/3). Black numbers denote the tunneling splitting of the components of the non-Kramers doublets. The presented results correspond to the CASSCF/NEVPT2-based calculations

Table S10. Crystal field B_k^q parameters of the ground atomic multiplet J = 15/2 of **Dy1**, calculated at SA-CASSCF(9,7)/NEVPT2/QDPT/Single-Aniso level.

B_k^q		k					
		2	4	6	8	10	12
q	-12						0.137 E-11
	-11						-0.592 E-11
	-10					-0.119 E-09	-0.574 E-12
	-9					-0.380 E-09	-0.587 E-12
	-8				-0.109 E-06	0.892 E-09	-0.433 E-11
	-7				-0.126 E-06	0.531 E-09	-0.219 E-11
	-6			0.224 E-04	-0.793 E-08	-0.371 E-10	0.256 E-12
	-5			0.128 E-03	-0.489 E-07	-0.965 E-10	0.341 E-11
	-4		-0.504 E-02	-0.197 E-04	0.367 E-07	-0.403 E-09	0.285 E-12
	-3		0.146 E-01	0.790 E-04	-0.195 E-06	-0.106 E-08	0.209 E-11
	-2	-0.691	0.108 E-02	0.183 E-04	-0.175 E-06	0.683 E-10	0.396 E-11
	-1	-1.934	0.128 E-01	0.170 E-05	-0.436 E-07	0.340 E-09	0.305 E-12
	0	-4.900	-0.106 E-01	0.559 E-04	-0.114 E-07	-0.911 E-10	0.179 E-12
	1	1.051	-0.423 E-02	-0.523 E-04	0.406 E-07	0.129 E-09	-0.102 E-11
	2	-0.123	0.127 E-02	0.199 E-04	-0.739 E-07	-0.559 E-10	0.223 E-11
	3		0.403 E-02	0.236 E-04	-0.210 E-07	-0.468 E-09	0.353 E-12
	4		-0.198 E-01	-0.743 E-04	0.135 E-06	-0.176 E-08	0.697 E-12
	5			-0.122 E-03	0.154 E-06	0.151 E-09	-0.526 E-11
	6			0.512 E-05	-0.105 E-07	-0.154 E-11	-0.151 E-12
	7				-0.468 E-08	0.635 E-10	-0.771 E-12
	8				-0.207 E-06	0.168 E-08	-0.731 E-11
	9					0.416 E-09	0.241 E-11
	10					0.210 E-09	-0.200 E-11
	11						0.352 E-12
	12						0.144 E-11

Table S11. Crystal field B_k^q parameters of the ground atomic multiplet J = 15/2 of **Dy2**, calculated at SA-CASSCF(9,7)/NEVPT2/QDPT/Single-Aniso level.

B_k^q		k					
		2	4	6	8	10	12
q	-12						0.261 E-11
	-11						-0.949 E-12
	-10					0.130 E-09	-0.152 E-11
	-9					-0.430 E-09	-0.202 E-11
	-8				-0.442 E-07	0.333 E-09	-0.135 E-11
	-7				-0.116 E-06	0.540 E-09	-0.295 E-11
	-6			0.595 E-05	0.127 E-09	-0.208 E-11	-0.968 E-14
	-5			0.260 E-04	0.174 E-06	-0.461 E-10	-0.191 E-11
	-4		0.193 E-01	0.956 E-04	-0.108 E-06	0.751 E-09	0.158 E-12
	-3		-0.647 E-03	-0.238 E-04	0.783 E-07	0.223 E-09	-0.964 E-12
	-2	-0.121	-0.762 E-04	-0.919 E-05	0.158 E-08	0.910 E-10	-0.704 E-12
	-1	1.349	-0.596 E-02	-0.589 E-04	0.482 E-07	0.121 E-09	-0.115 E-11
	0	-4.925	-0.107 E-01	0.524 E-04	-0.108 E-07	-0.675 E-10	0.137 E-12
	1	0.326	-0.466 E-02	0.483 E-04	-0.203 E-07	-0.232 E-09	0.881 E-12
	2	0.114	0.561 E-03	0.369 E-05	-0.134 E-07	-0.322 E-10	0.630 E-12
	3		-0.102 E-01	-0.458 E-04	0.117 E-06	0.783 E-09	-0.946 E-12
	4		0.126 E-02	0.712 E-05	-0.311 E-08	0.403 E-10	0.116 E-12
	5			-0.121 E-03	0.972 E-07	0.179 E-09	-0.517 E-11
	6			-0.768 E-05	-0.439 E-09	0.182 E-10	0.385 E-13
	7				-0.239 E-07	0.192 E-09	-0.146 E-11
	8				-0.285 E-06	-0.212 E-08	0.849 E-11
	9					-0.162 E-09	-0.475 E-13
	10					0.545 E-10	-0.526 E-12
	11						-0.434 E-11
	12						0.552 E-12

Table S12. Crystal field B_k^q parameters of the ground atomic multiplet J = 15/2 of **Dy3**, calculated at SA-CASSCF(9,7)/NEVPT2/QDPT/Single-Aniso level.

B_k^q		k					
		2	4	6	8	10	12
q	-12						-0.116 E-11
	-11						0.315 E-11
	-10					-0.299 E-10	-0.361 E-12
	-9					-0.158 E-09	-0.163 E-11
	-8				0.227 E-06	-0.170 E-08	0.707 E-11
	-7				0.146 E-07	-0.381 E-10	0.104 E-12
	-6			0.986 E-05	-0.885 E-08	0.133 E-10	-0.824 E-13
	-5			-0.300 E-04	-0.733 E-07	0.877 E-10	-0.632 E-12
	-4		-0.190 E-01	-0.949 E-04	0.141 E-06	-0.102 E-08	-0.525 E-12
	-3		0.688 E-02	0.241 E-04	-0.894 E-07	-0.213 E-09	0.599 E-12
	-2	0.669	0.723 E-03	-0.354 E-04	0.182 E-06	0.302 E-10	-0.516 E-11
	-1	0.652	-0.313 E-03	-0.800 E-04	0.563 E-07	0.267 E-09	-0.168 E-11
	0	-4.628	-0.105 E-01	0.523 E-04	-0.895 E-08	-0.692 E-10	0.126 E-12
	1	0.652	-0.347 E-02	-0.163 E-04	0.246 E-07	-0.143 E-10	-0.588 E-12
	2	-0.328	0.349 E-04	0.222 E-05	-0.296 E-07	0.614 E-12	0.128 E-12
	3		0.393 E-02	0.979 E-05	-0.764 E-08	-0.460 E-09	0.280 E-12
	4		0.725 E-02	0.380 E-04	-0.351 E-07	0.119 E-09	0.220 E-12
	5			0.727 E-04	0.574 E-07	-0.421 E-09	0.854 E-11
	6			0.102 E-04	-0.501 E-07	0.141 E-09	-0.428 E-12
	7				0.114 E-06	-0.558 E-09	0.306 E-11
	8				0.224 E-06	-0.176 E-08	0.718 E-11
	9					-0.125 E-09	0.574 E-12
	10					0.620 E-10	0.605 E-12
	11						-0.243 E-12
	12						0.300 E-11

Table S13. Crystal field B_k^q parameters of the ground atomic multiplet J = 6 of **Tb1**, calculated at SA-CASSCF(8,7)/NEVPT2/QDPT/Single-Aniso level.

B_k^q		k					
		2	4	6	8	10	12
q	-12						-0.802 E-11
	-11						-0.458 E-10
	-10					-0.932 E-09	0.389 E-11
	-9					0.134 E-08	0.271 E-10
	-8				0.528 E-06	-0.236 E-08	0.363 E-10
	-7				0.131 E-05	0.158 E-09	0.455 E-10
	-6			0.561 E-05	-0.157 E-06	0.410 E-09	-0.205 E-10
	-5			-0.634 E-03	0.173 E-04	-0.213 E-07	-0.473 E-09
	-4		-0.243 E-01	0.107 E-03	-0.157 E-05	0.283 E-07	-0.494 E-10
	-3		-0.779 E-01	0.369 E-03	-0.784 E-05	0.257 E-07	0.620 E-10
	-2	-0.594	0.270 E-01	-0.302 E-03	0.580 E-05	-0.990 E-08	-0.627 E-09
	-1	-8.185	0.107	-0.843 E-03	0.206 E-05	-0.142 E-07	-0.365 E-09
	0	-7.167	0.174 E-01	-0.319 E-04	-0.119 E-06	0.356 E-08	-0.572 E-10
	1	-2.706	0.337 E-01	-0.229 E-03	0.186 E-06	0.370 E-08	-0.264 E-09
	2	-0.727 E-02	-0.195 E-01	0.191 E-03	-0.339 E-05	0.938 E-08	-0.481 E-09
	3		0.479 E-01	-0.209 E-03	0.266 E-05	0.176 E-07	-0.668 E-10
	4		-0.435 E-01	0.150 E-03	-0.184 E-05	0.500 E-07	-0.287 E-09
	5			0.743 E-04	-0.146 E-05	0.218 E-08	0.377 E-10
	6			0.672 E-04	-0.265 E-06	0.391 E-09	0.619 E-10
	7				-0.172 E-05	0.147 E-07	-0.137 E-09
	8				0.329 E-06	-0.340 E-08	0.159 E-10
	9					-0.272 E-08	-0.180 E-10
	10					-0.121 E-08	-0.107 E-10
	11						0.397 E-10
	12						0.224 E-11

Table S14. Crystal field B_k^q parameters of the ground atomic multiplet J = 6 of **Tb2**, calculated at SA-CASSCF(8,7)/NEVPT2/QDPT/Single-Aniso level.

B_k^q		k					
		2	4	6	8	10	12
q	-12						0.941 E-11
	-11						0.114 E-10
	-10					0.885 E-09	0.119 E-10
	-9					0.433 E-08	0.338 E-10
	-8				0.413 E-06	-0.153 E-08	0.274 E-10
	-7				-0.382 E-06	0.786 E-08	-0.444 E-10
	-6			0.329 E-04	-0.867 E-07	0.215 E-10	0.374 E-10
	-5			0.341 E-03	-0.864 E-05	0.107 E-07	0.535 E-09
	-4		0.170 E-01	-0.690 E-04	0.964 E-06	-0.160 E-07	0.117 E-10
	-3		0.166 E-02	0.307 E-06	0.647 E-06	-0.835 E-08	-0.424 E-10
	-2	-0.197	0.998 E-02	-0.975 E-04	0.208 E-05	-0.561 E-08	0.302 E-09
	-1	-2.030	0.257 E-01	-0.191 E-03	0.653 E-06	-0.762 E-08	0.267 E-10
	0	-6.848	0.197 E-01	-0.391 E-04	-0.892 E-07	0.332 E-08	-0.648 E-10
	1	-8.308	0.105	-0.774 E-03	0.188 E-05	-0.133 E-07	-0.325 E-09
	2	-0.964	0.309 E-01	-0.363 E-03	0.735 E-05	-0.144 E-07	-0.428 E-09
	3		-0.741 E-01	0.335 E-03	-0.559 E-05	-0.208 E-07	0.157 E-09
	4		0.486 E-01	-0.157 E-03	0.214 E-05	-0.519 E-07	0.242 E-09
	5			0.553 E-03	-0.151 E-04	0.183 E-07	0.946 E-09
	6			0.339 E-04	-0.821 E-09	0.609 E-10	0.496 E-10
	7				-0.150 E-05	0.117 E-07	-0.107 E-09
	8				0.536 E-06	-0.286 E-08	0.256 E-10
	9					0.192 E-08	0.411 E-10
	10					0.417 E-09	0.104 E-10
	11						-0.225 E-10
	12						0.531 E-11

Table S15. Crystal field B_k^q parameters of the ground atomic multiplet J = 6 of **Tb3**, calculated at SA-CASSCF(8,7)/NEVPT2/QDPT/Single-Aniso level.

B_k^q		k					
		2	4	6	8	10	12
q	-12						-0.159 E-11
	-11						-0.860 E-11
	-10					0.121 E-08	0.135 E-10
	-9					-0.241 E-09	-0.343 E-10
	-8				-0.580 E-06	0.136 E-08	-0.841 E-11
	-7				-0.132 E-05	0.222 E-08	-0.829 E-10
	-6			0.505 E-04	-0.114 E-06	0.106 E-08	0.558 E-10
	-5			0.209 E-03	-0.619 E-05	0.681 E-08	-0.101 E-09
	-4		-0.448 E-01	0.122 E-03	-0.181 E-05	0.507 E-07	-0.260 E-09
	-3		0.258 E-01	-0.746 E-04	-0.878 E-06	0.335 E-07	-0.175 E-10
	-2	-0.376	0.819 E-02	-0.120 E-03	0.236 E-05	-0.242 E-08	-0.348 E-09
	-1	-10.494	0.123	-0.816 E-03	0.171 E-05	-0.111 E-08	-0.596 E-09
	0	-5.969	0.168 E-01	-0.511 E-05	-0.177 E-06	0.402 E-08	-0.443 E-10
	1	0.165	-0.299 E-02	0.612 E-04	-0.451 E-06	0.619 E-08	-0.270 E-10
	2	0.433	-0.329 E-01	0.346 E-03	-0.650 E-05	0.945 E-08	0.534 E-09
	3		0.788 E-01	-0.357 E-03	0.658 E-05	-0.995 E-08	0.133 E-10
	4		0.237 E-01	-0.648 E-04	0.119 E-05	-0.318 E-07	0.154 E-09
	5			0.485 E-03	-0.143 E-04	0.177 E-07	-0.335 E-09
	6			-0.214 E-04	0.186 E-06	-0.949 E-09	-0.229 E-10
	7				0.110 E-05	-0.133 E-07	0.606 E-10
	8				-0.381 E-06	0.239 E-08	0.415 E-12
	9					0.815 E-09	0.592 E-10
	10					0.848 E-09	0.137 E-10
	11						-0.481 E-10
	12						-0.126 E-10

References

1. F. Aquilante, J. Autschbach, A. Baiardi, S. Battaglia, V. A. Borin, L. F. Chibotaru, I. Conti, L. De Vico, M. Delcey, I. F. Galván, N. Ferré, L. Freitag, M. Garavelli, X. Gong, S. Knecht, E. D. Larsson, R. Lindh, M. Lundberg, P. Å. Malmqvist, A. Nenov, J. Norell, M. Odelius, M. Olivucci, T. B. Pedersen, L. Pedraza-González, Q. M. Phung, K. Pierloot, M. Reiher, I. Schapiro, J. Segarra-Martí, F. Segatta, L. Seijo, S. Sen, D. C. Sergentu, C. J. Stein, L. Ungur, M. Vacher, A. Valentini and V. Veryazov, Modern quantum chemistry with [Open]Molcas, *J. Chem. Phys.*, 2020, **152**, 214117.

2. a) F. Neese, F. Wennmohs, U. Becker and C. Riplinger, The ORCA Quantum Chemistry Program Package. *J. Chem. Phys.* 2020, *152* (22), 224108; b) F. Neese, Software Update: The ORCA Program System – Version 5.0. *WIREs Comput. Mol. Sci.* 2022, *12* (5), e1606.

3. P. Å. Malmqvist and B. O. Roos, The CASSCF state interaction method, *Chem. Phys. Lett.*, 1989, **155**, 189 – 194.

4. P. E. M. Siegbahn, J. Almlöf, A. Heiberg and B. O. Roos, The complete active space SCF(CASSCF) method in a Newton–Raphson formulation with application to the HNO molecule, *J. Chem. Phys.*, 1981, **74**, 2384 - 2396.

5. a) B. O. Roos, R. Lindh, K. Malmqvist, V. Veryazov, P.-O. Widmark, Main Group Atoms and Dimers Studied with a New Relativistic ANO Basis Set, *J. Phys. Chem. A*, 2004, **108**, 2851 – 2858; b) B.O. Roos, R. Lindh, P.A. Malmqvist, V. Veryazov and P.O. Widmark, New relativistic ANO basis sets for transition metal atoms, *J. Phys. Chem. A* 2005, **109**, 6575 – 6579.

6. a) D. A. Pantazis and F. Neese, All-electron basis sets for heavy elements, *WIREs Comput. Mol. Sci.* **2014**, *4*, 363 – 374; b) D. Aravena, F. Neese, D. A. Pantazis, Improved Segmented All-Electron Relativistically Contracted Basis Sets for the Lanthanides, *J. Chem. Theory Comput. 2016*, **1***2*, 1148 – 1156.

7. a) M. Douglas and N. M. Kroll, Quantum electrodynamical corrections to the fine structure of helium, *Ann. Phys.*, 1974, **82**, 89–155; b) B. A. Hess, Relativistic electronic-structure calculations employing a two-component no-pair formalism with external-field projection operators, *Phys. Rev. A*, 1986, **33**, 3742–.

8. a) P. Å. Malmqvist, B. O. Roos and B. Schimmelpfennig, The restricted active space (RAS) state interaction approach with spin–orbit coupling, *Chem. Phys. Lett.*, 2002, **357**, 230–240; b) B. O. Roos and P. Å. Malmqvist, Relativistic quantum chemistry: the multiconfigurational approach, *Phys. Chem. Chem. Phys.*, 2004, **6**, 2919–2927.

9. H. Nakano, R. Uchiyama and K. Hirao, Quasi-degenerate perturbation theory with general multiconfiguration self-consistent field reference functions, *J. Comput. Chem*, 2002, **23**. 1166 – 1175.

10. a) C. Angeli, R. Cimiraglia, S. Evangelisti, T. Leininger, J.-P. Malrieu, *J. Chem. Phys*. **2001**, *114*, 10252 – 10264; b) C. Angeli, R. Cimiraglia, J.-P. Malrieu, *J. Chem. Phys*. **2002**, *117*, 9138 – 9153.

11. a) L. F. Chibotaru, L. Ungur, Ab initio calculation of anisotropic magnetic properties of complexes. I. Unique definition of pseudospin Hamiltonians and their derivation, *J. Chem. Phys.*, 2012, **137**, 064112; b) L. Ungur, L. F. Chibotaru, *Computational Modelling of the Magnetic Properties of Lanthanide Compounds*, John Wiley & Sons, Ltd, 2015.

12. L. Ungure, L. F. Chibotaru, Strategies toward High-Temperature Lanthanide-Based Single-Molecule Magnets, *Inorg. Chem*. **2016**, *55*, 10043 – 10056.

13. J.-L. Liu, Y.-C. Chen and M.-L. Tong, Symmetry strategies for high performance lanthanide-based single-molecule magnets, *Chem. Soc. Rev.* 2018, **47**, 2431 – 2453.

14. A. Kramida, Yu. Ralchenko, J. Reader, and NIST ASD Team, NIST Atomic Spectra Database, Version 5.3, 2015. National Institute of Standards and Technology (NIST), Gaithersburg, MD, USA. URL: http://physics.nist.gov/asd.